
Article:
Burgess, I. orcid.org/0000-0001-9348-2915 and Sahin, M. (2018) Tensile membrane action of lightly-reinforced rectangular composite slabs in fire. Structures, 16. pp. 176-197. ISSN 2352-0124

https://doi.org/10.1016/j.istruc.2018.09.011

TENSILE MEMBRANE ACTION OF LIGHTLY-REINFORCED RECTANGULAR COMPOSITE SLABS IN FIRE

Ian Burgess* and Mesut Sahin

Department of Civil and Structural Engineering, University of Sheffield, Sheffield S1 3JD, United Kingdom

(*email: *ian.burgess@sheffield.ac.uk*)

ABSTRACT

A recently developed method of treating tensile membrane action of lightly reinforced concrete slabs, based on a rigorous treatment of the kinematics of movement of the yield-line mechanism, has been developed to consider composite slabs with unprotected downstand steel beams in fire conditions. The fire case differs from the enhancement of load capacity of slabs at ambient temperature in the respect that the applied loading is kept constant at a predetermined value, but the strength of the downstand beams progressively declines as their temperature rises. It is assumed that the concrete slab does not become hot enough in its active levels, within the duration of a fire, to reduce its strength. This extension to the method is derived systematically. It is seen that the yield line mechanisms of these slabs are aligned differently from those of the equivalent concrete slabs, so it is not valid to use the latter as the basis of a design calculation. The advantage of finite deflection due to tensile membrane action manifests itself as an enhancement of the steel beam temperature that can be sustained, above that at which the yield line mechanism forms. The peak enhancement occurs at the point at which reinforcing mesh begins to fracture progressively along diagonal yield lines. This fracture can be delayed and the peak temperature increased if the mesh ductility across the yield line cracks is increased by reducing the bond between bars and concrete, thus facilitating the bar-slip from the crack-faces. The effects of using meshes of different ductility classes, and both plain and deformed bars, are considered for composite slabs of different aspect ratios.

Key Words: *composite slabs, fire, tensile membrane action, yield line theory*

Notation List

A_1, A_{2y}, A_{2x}	Concrete stress block areas on diagonal and central yield lines.
B_T	Temperature-dependent total tensile capacity of all the downstand steel beams.
C	Concrete resultant force across a diagonal yield line.
C_{x2}, C_{y2}	Concrete x- or y- direction resultant forces on central yield line.
d_b	Bar diameter.
f_c, f_{cm}	Concrete strength.
f_{px}, f_{py}	Steel mesh strengths per unit width in x and y directions.
f_y, f_u	Steel mesh yield and ultimate stresses.
f_s, f_b	General reinforcing bar stress and bar stress crossing yield line crack.
l	y-dimension of slab.
l_d, l'_d	Elastic and plastic bond development lengths.
M_B	Moment of beam forces about y-aligned edge.
M_{CS}, M'_{CS}	Moments including C and S about y-aligned or x-aligned edge respectively.
M_{Cx2}, M'_{Cy2}	Moments of C_{x2}, C_{y2} about y-aligned or x-aligned edge respectively.
M_{ext}, M'_{ext}	Total external moment about y-aligned or x-aligned edge respectively.
$M_{\text{int}}, M'_{\text{int}}$	Total internal moment about y-aligned or x-aligned edge respectively.
M_{Tx1}, M_{Tx2}	Moments of T_{x1}, T_{x2} about y-aligned edge.
M'_{Ty1}, M'_{Ty2}	Moments of T_{y1}, T_{y2} about x-aligned edge.
M_V	Moment of V about appropriate edge (depends on facet considered).
n_b	Number of unprotected downstand beams across the y-dimension of the slab.
n_d	Number of unprotected downstand beams crossing a diagonal yield line.
n_m	Number of unprotected downstand beams crossing central yield line.
n_{mid}	Value 1 if unprotected downstand beam on centre line of slab, 0 otherwise.
n_x, n_y	Dimensionless coordinates of yield line intersection in x- and y-aligned mechanisms.
p	Distributed load intensity on slab.
r	Aspect ratio of slab (x:y).
S	Resultant horizontal shear force along a diagonal yield line.
s_b	Bar spacing in isotropic welded mesh.
t	Thickness of slab.
T_{x1}, T_{x2}	Tensile resultant forces in x-aligned mesh.
T_{y1}, T_{y2}	Tensile resultant forces in y-aligned mesh.
u, v	Movements of a point on a crack-face in x and y directions.

u_b, u_b'	Elastic and plastic bond stresses.
V	Resultant vertical shear force across a diagonal yield line.
x, y, z	Coordinate system: parallel and perpendicular to downstand beams, and through depth of slab.
$x_{CA,1}$, $y_{CA,1}$, $z_{CA,1}$	Coordinates of concrete stress-block centroids on diagonal and central yield lines.
$x_{lim,1y}$	Limiting x coordinate of unbroken y-direction reinforcement.
$x_{t,1}$	x coordinate at which y reinforcement emerges from compressive stress block.
$y_{lim,1x}$	Limiting y coordinate of unbroken x-direction reinforcement.
$y_{t,1}$	y coordinate at which x reinforcement emerges from compressive stress block.
z_1, z_2	Depths of concrete stress block at slab corner and yield line intersection.
β	Dimensionless strength ratio $\beta = \dfrac{B_T}{f_c l^2}$
γ	Angle of diagonal yield line to y axis.
δ_A	Deflection of centre of slab.
$\varepsilon_s, \varepsilon_u, \varepsilon_y$	Reinforcing bar strains: general, ultimate, yield.
Δ_x, Δ_y	x and y movements of facets at corner of slab
$\Delta_{lim,x}, \Delta_{lim,y}$	Limiting *x* and *y* crack widths at which reinforcement fractures.
η_x, η_y	Dimensionless limiting crack widths $\eta_x = \dfrac{\Delta_{lim,x}}{l}$ and $\eta_y = \dfrac{\Delta_{lim,y}}{l}$
θ	Rotation of slab Facet 1 about x axis.
ϕ	Rotation of slab Facet 2 about y axis.
μ	Mesh depth as a proportion of slab thickness.
λ_x, λ_y	Dimensionless strength ratios $\lambda_x = \dfrac{f_{px}}{f_c l}$ and $\lambda_y = \dfrac{f_{py}}{f_c l}$
ψ_1, ψ_2	Dimensionless stress block depths $\psi_1 = z_1 / l,\ \psi_2 = z_2 / l$
τ	Dimensionless slab thickness *t/l*

TENSILE MEMBRANE ACTION OF LIGHTLY-REINFORCED RECTANGULAR COMPOSITE SLABS IN FIRE

Ian Burgess and Mesut Sahin

1. INTRODUCTION

Tensile membrane action (TMA) is a large-deflection enhancement of the load capacity of initially flat plates, which are transversely supported around their edges. As its name suggests the enhancement derives from a progressive evolution of the transverse-load-carrying mechanism from one that involves only bending and torsion of cross-sections to one that also includes membrane stresses within the deflected profile. These membrane stresses aggregate to a net two-dimensional tension field, which is almost hydrostatic in the central region of the plate, surrounded by a net compression field which is circumferential between the tension field and the plate perimeter. This is self-equilibrating if the transverse support is maintained around the edges of the plate. This is observable in geometrically nonlinear numerical analysis of plates and thin concrete slabs, which are unrestrained against in-plane movement of their edges. Where these are restrained, then catenary tensions further enhance the plate capacity, but have to be resisted at the plate edges, so this mechanism is not internally equilibrating.

For reinforced concrete slabs, it is usually justifiable to base the analysis of TMA on an initial optimal yield-line mechanism [1, 2], which remains unchanged as the loading, and consequently the slab deflection, increases. This is especially the case for lightly reinforced slabs, for which the yield-line hinges involve essentially discrete cracks through the concrete thickness; once the concrete has fractured the plastic moment capacity at a hinge is much lower than the fracture moment of the uncracked section. The early work on TMA, based on the optimal yield-line mechanism, was carried out during the 1960s and early 1970s [3 - 11]; this work was described in an earlier paper [12] by the lead author, and will not be revisited in detail here. The work made virtually no impact on the structural design of concrete slabs, because the large deflections involved violate all normal serviceability limit state criteria in structural codes of practice.

Tensile membrane action has returned to research attention during the past two decades because of the need to design structures to avoid disproportionate collapse under hazard loadings of different types. In such cases, large deflections become unimportant if collapse is avoided. The most usual scenario involving local damage to a framed structure because of an explosive device or impact is loss of a single ground-floor column, requiring its vertical load to be redistributed through beams and slabs to adjacent columns. Since this increases at least some spans very considerably, large deflections are inevitable and TMA is one mechanism that can be utilized in certain damage scenarios to prevent collapse. In fire scenarios, TMA has been seen to prevent collapse of composite, rather than reinforced concrete, floors when the strength of their downstand steel secondary beams has been highly degraded at high temperature. The prime illustration of the effectiveness of TMA in preventing collapse of composite floors in intense fire conditions was in the full-scale fire tests at Cardington [13 – 15], which gave rise

to a fire engineering design strategy that can be used to optimize the usage of passive protection on downstand beams. In this strategy the necessary vertical support condition is established by protecting the primary and secondary beams on the column gridlines around the edges of a slab panel while leaving its internal secondary beams unprotected. This strategy is illustrated in Figure 1.

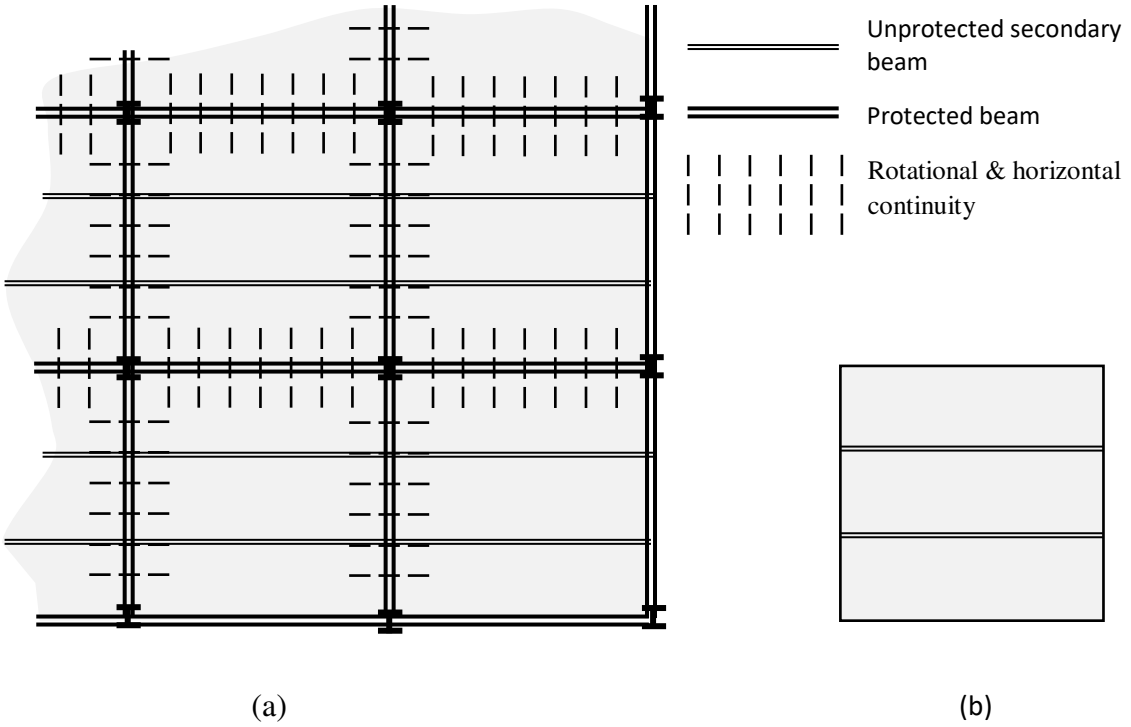

Figure 1: Protection strategy to utilize TMA for composite floors. (a) Continuity across protected beams; (b) Single slab-panel model.

It can be seen from Figure 1(a) that there is continuity across the protected beams except around the building perimeter. However, it is usually considered unsafe to make use of this continuity in design, because it is very likely that reinforcement will fracture over support beams due to high hogging moments; it is also impossible to guarantee that the slab will remain composite with the protected beams when this happens. Hence a rational design model is the single-panel one illustrated in Figure 1(b), which uses the transverse support provided by the edge beams, but ignores its in-plane and rotational restraint.

In the previous paper [12] the first author of this paper introduced a large-deflection treatment of the behaviour of thin, lightly reinforced concrete slabs after an initial yield-line mechanism has been formed at a certain load intensity. This rigid-plastic bending mechanism has infinitesimal deflection, and the optimal shape of the mechanism effectively fixes itself for the larger displacements, which cause TMA. This is true because the yield-line cracks for such lightly reinforced slabs are discrete, and the net bending strength of the slab away from a yield line is much higher than that at the yield line itself. The main emphases of this method are:

- To treat the kinematics of the flat slab facets separated by the yield lines correctly, so that each facet has a compatible rotation about its supported edge, and an in-plane (horizontal) movement perpendicular to this edge. In combination, these create zones of concrete contact or separation on each yield line. The contact zones are either rectangular, triangular or trapezoidal, and change continuously as the transverse deflections increase.
- To compute the in-plane movements of the facets from horizontal equilibrium of the resultant forces acting on the slab facets. These forces derive from the strength of the concrete areas of the contact zones and the net plastic tensile forces of the unbroken reinforcing mesh across the yield lines.
- To allow the orthogonal mesh bars in each direction to fracture at the point where the crack-width resolved into the appropriate direction reaches a given value.
- To establish transverse equilibrium by equilibrating the transverse forces and external load at high deflections.

The fact that mesh can fracture across yield lines creates a natural limit to the enhancement of yield-line capacity that can be generated. The key parameter in making TMA effective is then the ductility of rebar between the faces of a discrete crack; higher ductility gives higher enhancement of capacity.

2. MODELLING THE COMPOSITE SLAB IN FIRE

Although based on the same principles of the kinematics and horizontal equilibrium of an optimal yield-line mechanism at finite deflection, the analysis of a composite slab with parallel downstand steel beams differs from that of lightly reinforced plain concrete slabs in the respect that elevated temperatures now play a key part. The analysis introduced previously considers the enhancement of a slab's ambient-temperature yield-line load capacity due to finite deflection without considering the effect of fire heating. For thin plain concrete slabs, which have low effective depths and are heated from below, the temperature of the reinforcing mesh stays below values that would cause any weakening for a very long time, given the extent of its lower cover and the relatively low thermal conductivity of concrete. It is unlikely that a slab of this type would be appropriate to carry normal floor loading intensities for either ultimate or serviceability limit states. However, it is inherently suitable to carry the compression force that balances the tension in the whole cross-sectional area of a downstand steel section, together constituting the "flanges" of a composite beam in sagging. In fire conditions, the floor loading remains constant. The temperatures of either unprotected or protected downstand steel beams rise relatively quickly compared with that of the mesh in the concrete slab, progressively reducing the strength of these composite sections. At a critical temperature, the strength of the downstand beams will have been degraded to the point at which a yield-line mechanism forms in the composite slab. At any higher steel beam temperature, its further reduction in strength must be compensated by a contribution from tensile membrane action at some finite deflection of the yield-line pattern created at the critical temperature.

The effect of tensile membrane action can therefore be expressed as the deflection required for the slab panel to carry the applied load at any steel temperature level.

The effects of attaching downstand beams to a concrete slab panel are twofold. Firstly, the bending section becomes composite, with the steel section carrying tensile stress, and an effective width of the concrete slab acting solely in compression; this gives a greatly increased moment capacity compared with those of the two elements involved. Secondly, in terms of the combined areas of steel in either slab direction, it effectively makes the panel highly orthotropic, except at very high steel temperatures when its contribution becomes very small. The degree of orthotropy of a slab is one of the key parameters that determine the geometry of its optimum yield-line mechanism, including its alignment, and for a composite slab this depends on the critical steel temperature at which the mechanism forms. This change of yield-line mechanism is illustrated in Figure 2.

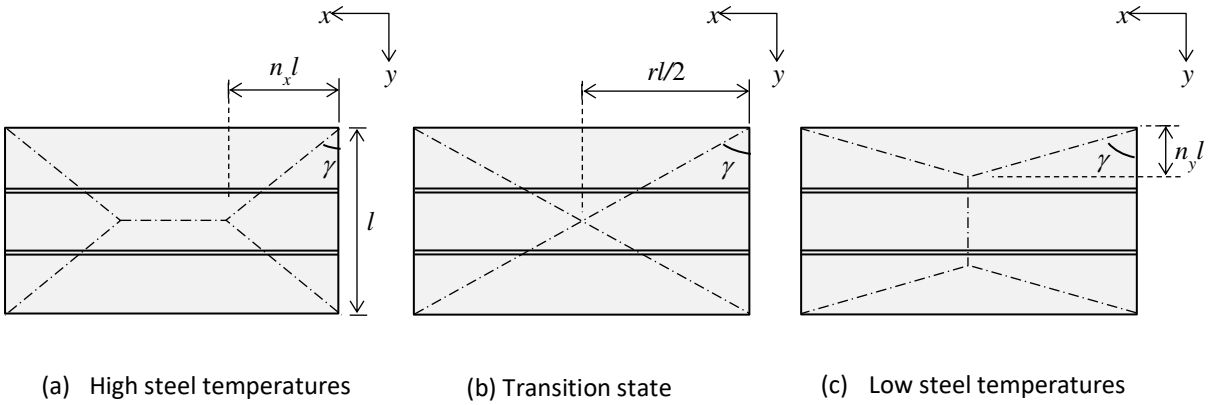

Figure 2: Changes in yield-line geometry for different critical steel section temperatures.

3. CRITICAL YIELD-LINE TEMPERATURE AND ITS ENHANCEMENT

As has been previously described, at some steel beam temperature the load capacity of a composite slab should decrease to the level of the applied load intensity and a pattern of yield lines forms; the only exception to this is when the slab is capable of carrying the applied load without the presence of the steel beams. If the steel beam temperature increases beyond this critical value, the geometry of the yield-line pattern is now fixed for further deflection. For rectangular slabs, the yield lines divide the slab into two triangular and two trapezoidal flat facets.

3.1. Forces across the yield lines

Prior to the formation of the yield lines at the critical steel temperature, neither the alignment of the mechanism nor the details of its geometry can be known, and so both possible alignments have to be investigated. The alignments will each be denoted in terms of the directions of their middle yield line. The essential details, including the force resultants along the yield lines, needed to establish equilibrium of the *x*- and *y*-aligned mechanisms are shown in Figures 3 and 4 respectively.

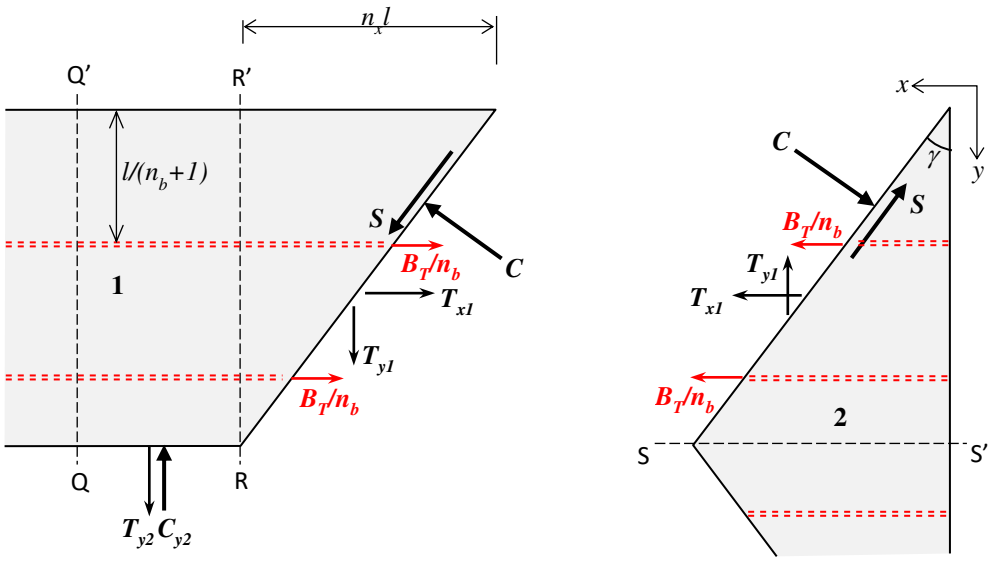

Figure 3: The horizontal force system between facets along the yield lines, for *x*-aligned mechanisms.

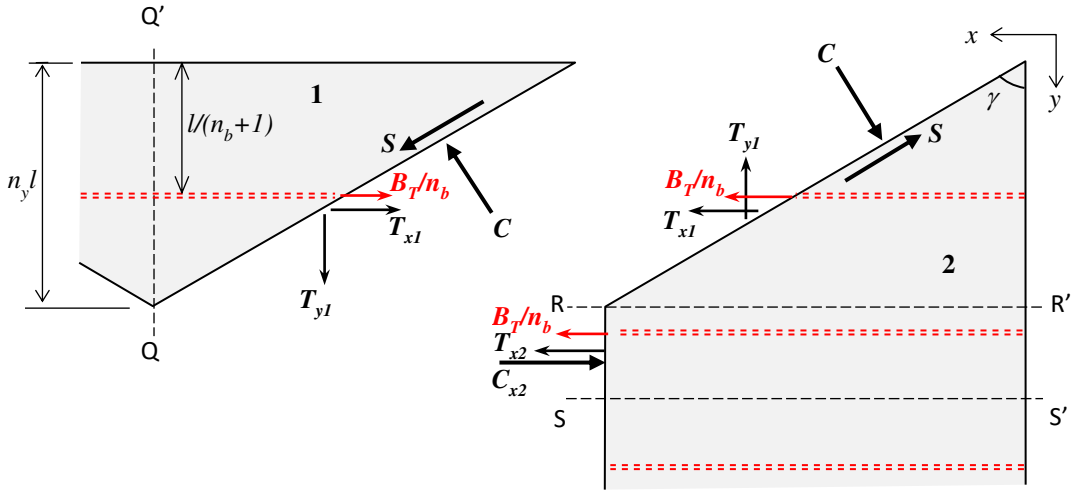

Figure 4: The horizontal force system between facets along the yield lines, for *y*-aligned mechanisms.

In these figures the compressive forces C, C_{x2} and C_{y2} are the resultant forces from the concrete stress blocks on the yield lines (half-length yield lines in the cases of C_{x2} and C_{y2}), assuming that the concrete acts with a uniform compressive strength. The tensile forces T_{x1}, T_{x2}, T_{y1} and T_{y2} are the resultants from the reinforcing mesh at yield, over the lengths within which it is unfractured and in tension. Shear forces S are present along the diagonal yield lines. There are n_b identical downstand steel beams aligned in the *x*-direction, uniformly spaced across the *y*-dimension of the slab at a spacing $l/(n_b+1)$. These are assumed to be unprotected and to be at the same temperature at any time, so that they each have a tensile force at the temperature-dependent yield strength of the structural steel. The total of these beam forces is denoted as B_T, so each individual beam force is denoted as B_T/n_b. It is assumed that the edges of the panel are vertically supported but do not have steel downstand beams attached.

3.2. Horizontal equilibrium of the facets

A pair of equilibrium equations can be generated for either type of yield-line mechanism by resolving the forces for Facet 1 in the *y*-direction and for Facet 2 in the *x*-direction. For the *x*-aligned mechanism this gives:

$$T_{y1} + T_{y2} = C\sin\gamma - S\cos\gamma + C_{y2} \tag{1}$$

$$T_{x1} + B_T / 2 = C\cos\gamma + S\sin\gamma \tag{2}$$

Eliminating *S* from Equations (1) and (2) gives:

$$(T_{x1} + B_T / 2)\cos\gamma + \left(T_{y1} + T_{y2}\right)\sin\gamma = C + C_{y2}\sin\gamma \tag{3}$$

For the *y*-aligned mechanism:

$$T_{y1} = C\sin\gamma - S\cos\gamma \tag{4}$$

$$T_{x1} + T_{x2} + B_T / 2 = C\cos\gamma + S\sin\gamma + C_{x2} \tag{5}$$

Eliminating *S* from Equations (4) and (5) gives:

$$(T_{x1} + T_{x2} + B_T / 2)\cos\gamma + T_{y1}\sin\gamma = C + C_{x2}\sin\gamma \tag{6}$$

These forces need to be related to the kinematics of the displacements and rotations of the two plate facets at any transverse displacement.

3.3. Kinematics of yield-line deflection

The kinematics of a deflecting rectangular slab panel, considered as flat facets connected at the yield line pattern has been covered in detail in the previous paper. At a small finite deflection δ_A of both types of facet, measured at the intersections of the yield lines, they interact with compatible angles of rotation θ and ϕ, and with rigid-body movements; Δ_x for Facet 2 and Δ_y for Facet 1. These rotations and movements are illustrated in Figure 5.

The rotations θ and ϕ are linked by:

$$\phi = \theta\tan\gamma = 2n_x\theta \tag{7}$$

for the *x*-aligned case, and

$$\phi = \theta\tan\gamma = \frac{r}{2n_y}\theta \tag{8}$$

For the *y*-aligned case.

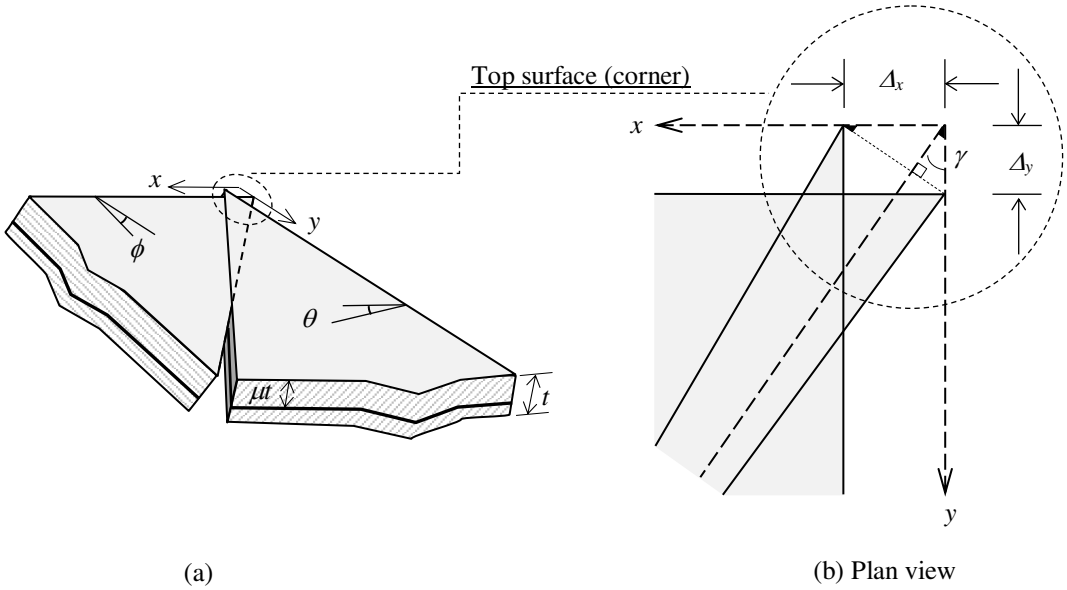

(a) (b) Plan view

Figure 5: Geometry of diagonal yield-line crack opening. (a) Crack opening at rebar level; (b) Top surface of slab, including rigid-body movements of triangular and trapezoidal slab facets.

A position along a diagonal yield line, located at zero deflection by x and y coordinates which are compatible with the angle γ, and by a depth z from the top-surface of the slab, separates at finite deflection into a point on the crack-surface of Facet 1, which can move by v in the y-direction and a point on the crack-surface of Facet 2 which moves by u in the x-direction.

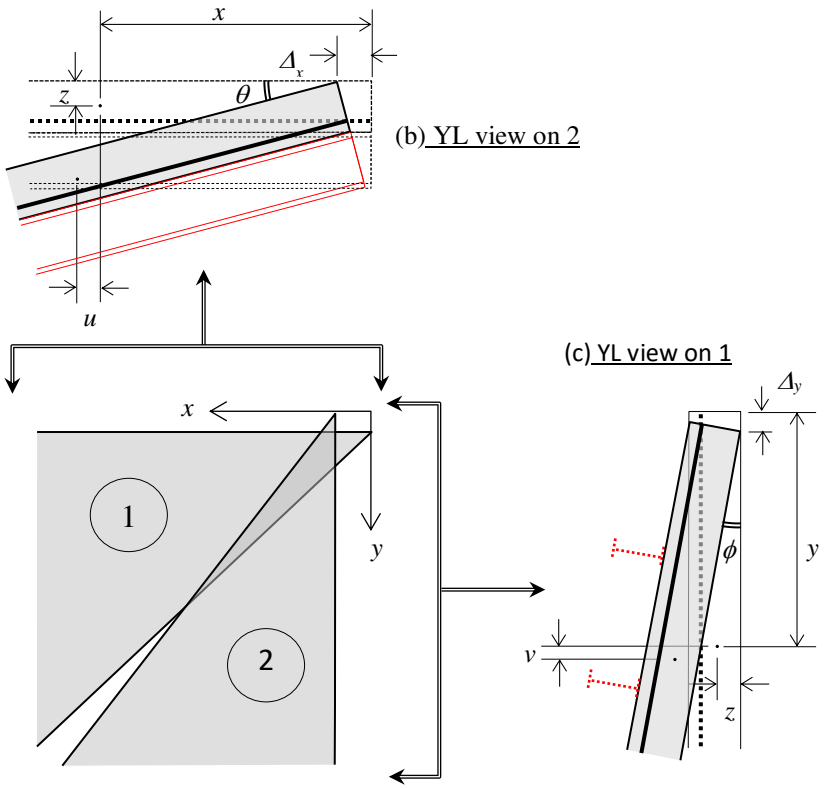

Figure 6: Movements of a point on a diagonal yield line. (a) Plan view of top surface of slab; (b) x-direction motion u on Facet 2; (c) y-direction motion v on Facet 1.

These movements are shown in Figure 6, and apply to either *x*- or *y*-aligned mechanisms.

The motions *u* and *v* are given by:

$$u = \Delta_x - \theta z - \frac{\theta^2 x}{2} \tag{9}$$

$$v = \Delta_y - \phi z - \frac{\phi^2 y}{2} \tag{10}$$

The equation of the neutral axis on each diagonal yield line is given by setting either $u = 0$ in Equation (9), or $v = 0$ in Equation (10), to indicate the position at which the facets cease to intersect. This gives the straight line:

$$z = \frac{\Delta_x}{\theta} - \frac{\theta x}{2} \tag{11}$$

The *z*-coordinates of the ends of the neutral axis, at the corner of the slab and at the intersection of the yield lines, are denoted as z_1 and z_2, given by setting *x* to zero and to the *x*-coordinate of the intersection, respectively.

For the *x*-aligned mechanism:

$$z_1 = \frac{\Delta_x}{\theta} \tag{12}$$

$$z_2 = \frac{\Delta_x}{\theta} - \frac{\theta n_x l}{2} = z_1 - \frac{\theta n_x l}{2} \tag{13}$$

For the *y*-aligned mechanism:

$$z_1 = \frac{\Delta_x}{\theta} \tag{14}$$

$$z_2 = \frac{\Delta_x}{\theta} - \frac{\theta r l}{4} = z_1 - \frac{\theta r l}{4} \tag{15}$$

The central yield line clearly retains the neutral axis depth at the intersection, z_2, along its length. Equations (12-15) clearly suggest that at zero deflection $z_1 = z_2$ so that the concrete compression stress block is a uniform-depth layer at the top of the slab. The normal assumption for traditional yield-line theory is that about each orthogonal direction in the slab there is a plastic moment capacity based on a stress-block depth, which is sufficient to balance the plastic tensile capacity of the normal reinforcing bars. For an orthotropic mesh (or for a composite slab) this implies different neutral axis depths for the two orthogonal directions; this is clearly a false assumption. Figure 7 shows the progressive change of the concrete stress block for an *x*-aligned mechanism as the deflection of the yield-line mechanism proceeds, with z_1 generally increasing and z_2 decreasing from their initial equal values.

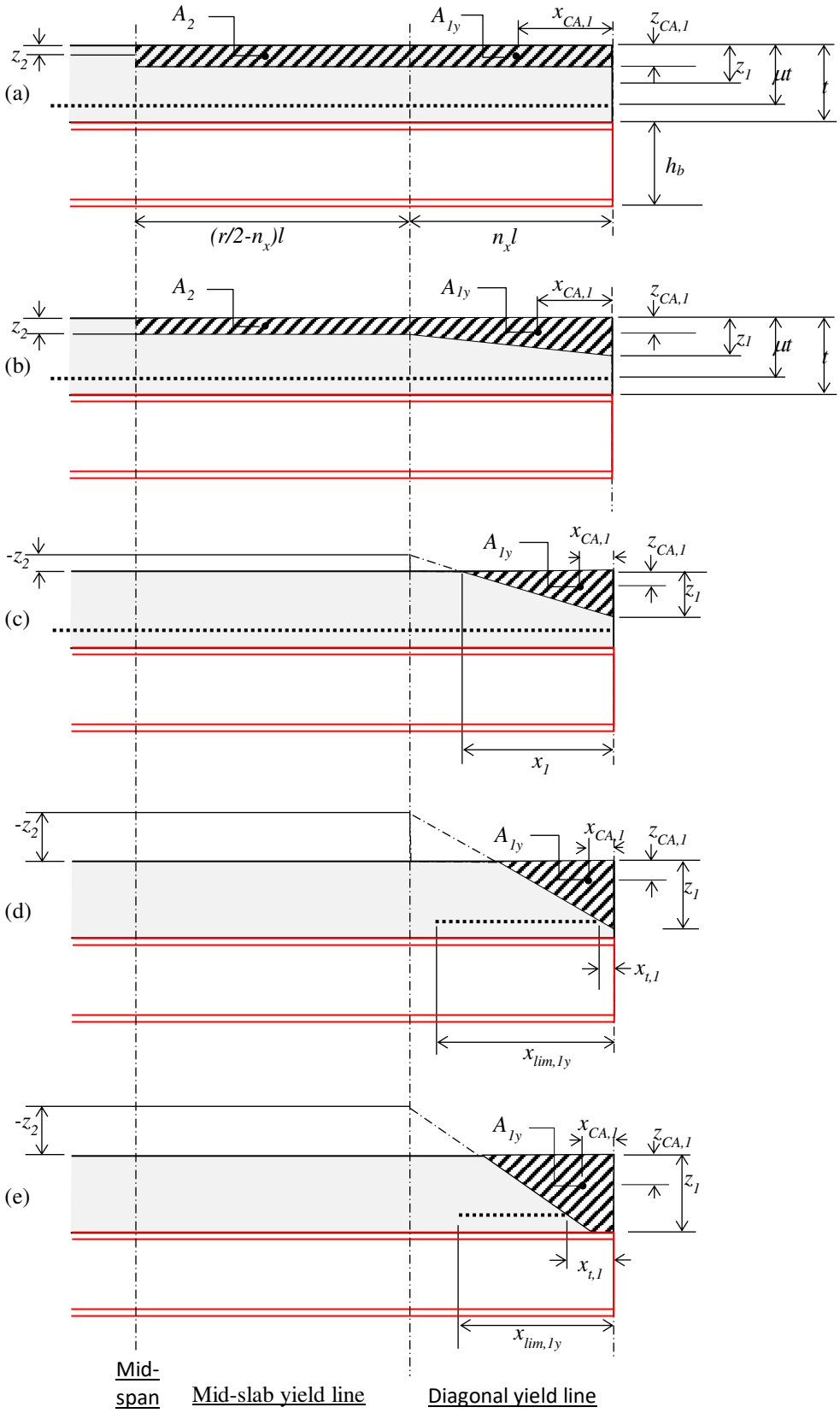

Figure 7: Projections of the yield line stress blocks at different stages for *x*-aligned mechanism: (a) uniform stress block at yield-line creation; (b) stress blocks on all yield lines; (c) Triangular stress blocks above rebar on diagonal yield lines; (d) Triangular stress blocks below rebar on diagonal yield lines; (e) Trapezoidal stress blocks on diagonal yield lines.

The stress block on the central yield line diminishes as z_2 decreases until it vanishes altogether when z_2 becomes negative. At this stage, the stress block on each diagonal yield line becomes triangular; under some circumstances, it may eventually become trapezoidal, as shown in Figure 7(e). Other special events are illustrated in Figure 7(d). Reinforcing mesh will fracture completely at some value of crack separation (which may differ for the two bar directions), and this fractured zone will change progressively as the deflection increases. A similar sequence also occurs for *y*-aligned mechanisms.

It is assumed that *x*- and *y*-direction reinforcing bars fracture at crack separations $\Delta_{lim,x}$ and $\Delta_{lim,y}$ respectively, at the levels of these bars. The values of these limiting crack-widths depend on the bars' fracture strain (ductility), by its bond relationship with the surrounding concrete and by the proximity of adjacent anchor-points such as welds to orthogonal bars. Alternatively, they may be based on experimental testing. The coordinates beyond which the bars are fractured can then be defined from the limiting crack-width at the level of the appropriate bars, using Equations (7-10):

For reinforcement in the *x*-direction the limiting coordinate for fracture is:

$$y_{lim,1x} = \frac{1}{n_x \theta}\left(z_1 + \frac{\Delta_{lim,x}}{\theta} - \mu t \right) \tag{16}$$

for the *x*-aligned mechanism, up to a maximum value of $l/2$, or:

$$y_{lim,1x} = \frac{4n_y}{r\theta}\left(z_1 + \frac{\Delta_{lim,x}}{\theta} - \mu t \right) \tag{17}$$

for the *y*-aligned mechanism, up to a maximum value of $n_y l$.

For reinforcement in the *y*-direction the limiting coordinate for fracture is:

$$x_{lim,1y} = \frac{2}{\theta}\left(z_1 + \frac{\Delta_{lim,y}}{2\theta n_x} - \mu t \right) \tag{18}$$

for the *x*-aligned mechanism, up to a maximum value of $n_x l$ or:

$$x_{lim,1y} = \frac{2}{\theta}\left(z_1 + \frac{2n_y \Delta_{lim,y}}{r\theta} - \mu t \right) \tag{19}$$

for the *y*-aligned mechanism, up to a maximum value of $rl/2$.

Clearly, when $x_{lim,1y} \le 0$ or $y_{lim,1x} \le 0$ then the corresponding bars have completely fractured across the diagonal yield lines.

In addition, when the concrete stress block crosses the depth of a layer of reinforcement, the bars that fall within the stress block become inactive. In this case the limiting coordinate at which mesh is no

longer in tension is:

$$y_{t,1} = \frac{1}{n_x \theta}\left(z_1 - \mu t\right) \tag{20}$$

for the *x*-aligned mechanism, and

$$y_{t,1} = \frac{4n_y}{r\theta}\left(z_1 - \mu t\right) \tag{21}$$

for the *y*-aligned mechanism. If the stress block lies above the mesh level then $y_{t,1} = 0$.

3.4. In-plane equilibrium

It is now possible to define the forces which maintain the in-plane equilibrium of the slab facets, given that the mesh is assumed to act at yield over the distances where the bars are intact and in tension, with strengths per unit width of f_{px} and f_{py}. Concrete within the stress blocks is assumed to act at its compressive strength f_c, with its resultant forces acting at the centroids of the stress blocks, which are shown on Figure 7. The individual force components shown in Figures 3 and 4 are given as follows:

For both alignments:

$$C = A_1 f_c \tag{22}$$

$$T_{y1} = \left(x_{lim,1y} - x_{t,1}\right) f_{py} \tag{23}$$

$$T_{x1} = \left(y_{lim,1x} - y_{t,1}\right) f_{px} \tag{24}$$

For the *x*-aligned mechanism (Figure 3):

$$T_{y2} = \left(r/2 - n_x\right) l f_{py} \quad \text{or } T_{y2} = 0 \tag{25}$$

$$C_{y2} = A_{2y} f_c \quad \text{or } C_{y2} = 0 \tag{26}$$

For the *y*-aligned mechanism (Figure 4):

$$T_{x2} = f_{px} l \left(\frac{1}{2} - n_y\right) \text{ or } T_{x2} = 0 \tag{27}$$

$$C_{x2} = f_c l \left(\frac{1}{2} - n_y\right)\left(z_1 - \frac{\theta r l}{4}\right) \text{ or } C_{x2} = 0 \tag{28}$$

The only other component of the in-plane equilibrium equations is the total longitudinal force B_T in the downstand steel beams, which is temperature-dependent.

Given these relationships, the in-plane equilibrium equations (3) and (6) at any specified steel beam temperature are functions of the rotation angle θ and the neutral axis depth z_1. At any specified deflection, defined by the angle θ, and steel beam temperature T, the in-plane equilibrium equation can be solved for z_1. This must be compatible with the assumptions made with respect to the value of z_2 and the widths of slab over which the reinforcing mesh is fractured.

3.5. Transverse equilibrium and load capacity

Vertical equilibrium, and hence the load capacity of the composite panel at high deflections, can easily be established by equating the external (load-induced) and internal moments within each of the two types of facet about their supported edges. There are equal and opposite resultant transverse shear forces between these facets at each of the diagonal yield lines, which do not affect the horizontal equilibrium equations given in Section 3.4. It is assumed for convenience (although it is irrelevant to the eventual solution) that these transverse shear forces act through the centroid of the concrete stress-block on the diagonal yield line. Because of the inherent symmetry there is no transverse shear force crossing the central yield line. The forces involved in the internal and external moments about the edge axis XX' for a *y*-aligned trapezoidal facet are shown in Figure 8(a) and about YY' for the corresponding triangular facet in Figure 8(b). The alternative, *x*-aligned, cases will be seen to be much less usual for practical design details, and are not specifically illustrated in the figures.

<u>*y*-aligned mechanism</u>

The equilibrium equation for a *y*-aligned trapezoidal facet can be aggregated from the individual internal moments, equated to the opposing external moments. The bottom edge of the concrete slab is selected as the level for the axes XX' and YY' about which these moments are calculated. The "internal" clockwise moments about YY' are:

$$M_{Tx1} = T_{x1}\left((x_{\lim,1x} + x_{T,1})\frac{\theta}{2} - t(1-\mu)(1-\frac{\theta^2}{2}) \right) \tag{29}$$

$$M_{Tx2} = T_{x2}\left(rl_y \frac{\theta}{2} - t(1-\mu)(1-\frac{\theta^2}{2}) \right) \tag{30}$$

$$M_{CS} = (C\cos\gamma_y + S\sin\gamma_y)\left(-x_{CA1}\theta + (t - z_{CA1})(1-\frac{\theta^2}{2}) \right) \tag{31}$$

$$M_{Cx2} = C_{x2}\left(-rl_y \frac{\theta}{2} + (t - \frac{z_2}{2})(1-\frac{\theta^2}{2}) \right) \tag{32}$$

$$M_V = V\left(-(t - z_{CA1})\theta - x_{CA1}(1-\frac{\theta^2}{2}) \right) \tag{33}$$

$$M_B = \frac{B_T}{n_B}\left(\sum_{i=1}^{n_d}\left(\frac{il_y \tan\gamma_y}{(n_B+1)}\theta + \frac{h}{2}(1-\frac{\theta^2}{2})\right) + n_m\left(\frac{rl_y}{2}\theta + \frac{h}{2}(1-\frac{\theta^2}{2})\right) + \frac{n_{mid}}{2}\left(\frac{rl_y}{2}\theta + \frac{h}{2}(1-\frac{\theta^2}{2})\right)\right) \quad (34)$$

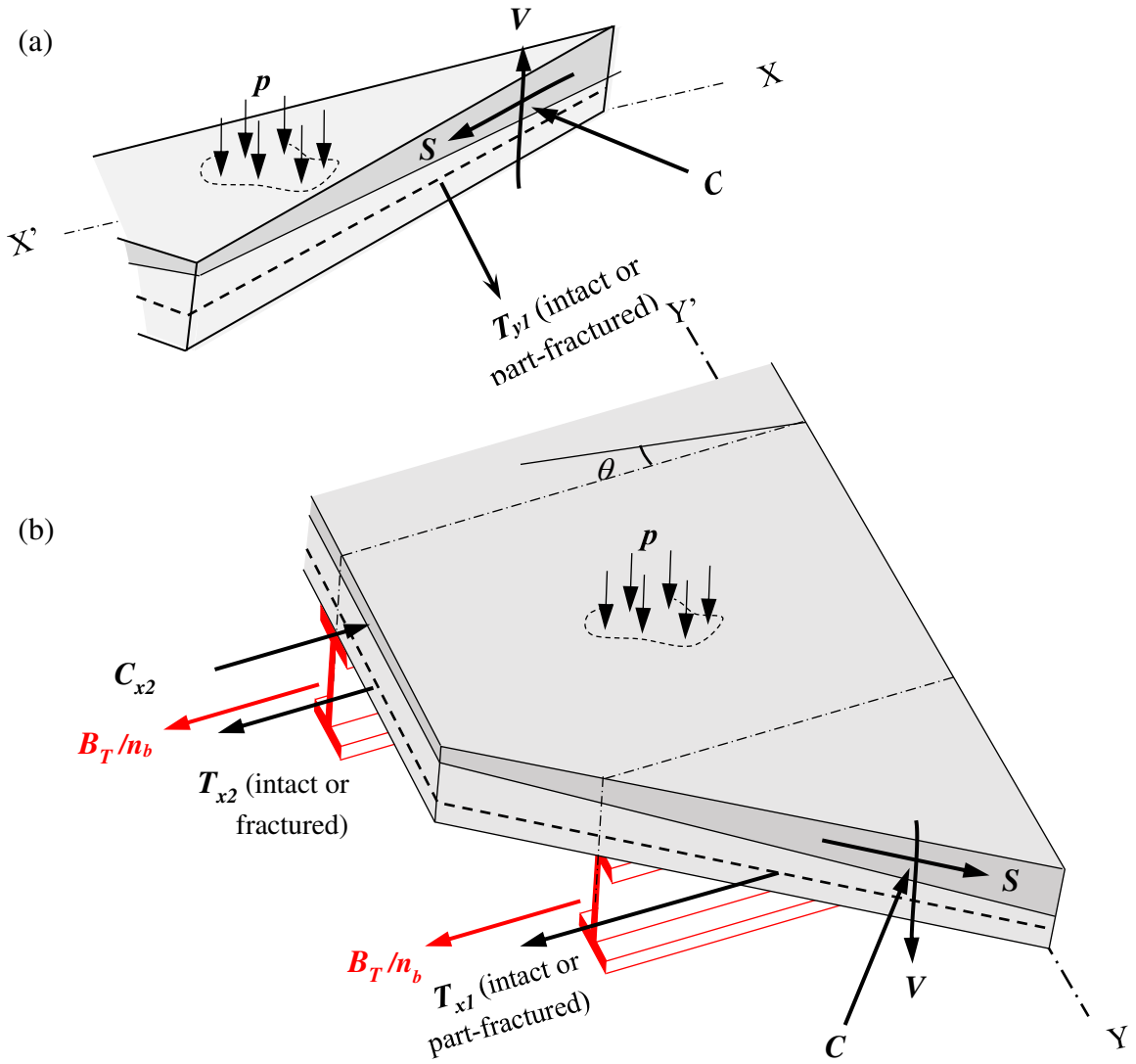

Figure 8: Forces involved in equilibrium of moments for triangular facet about the edge axis X'X", and for trapezoidal facet about edge axis Y'Y".

The complete "internal" moment is then:

$$M_{\text{int}} = M_{Tx1} + M_{Tx2} + M_{CS} + M_{Cx2} + M_V + M_B \quad (35)$$

The "external" moment about YY' is:

$$M_{Ext} = \frac{prl_y^2}{2}\left(\frac{n_y}{2}\left(t\theta + \frac{rl_y}{6}(1-\frac{\theta^2}{2})\right) + (\frac{1}{2}-n_y)\left(t\theta + \frac{rl_y}{4}(1-\frac{\theta^2}{2})\right)\right) \quad (36)$$

For the corresponding triangular facet the "internal" clockwise moments about XX' are:

$$M'_{Ty1} = T_{y1}\left((y_{\lim,1x} + y_{T,1})\frac{\phi}{2} - t(1-\mu)(1-\frac{\phi^2}{2}) \right) \tag{37}$$

$$M'_{CS} = -(C\sin\gamma_y - S\cos\gamma_y)\left(y_{CA1}\phi - (t - z_{CA1})(1-\frac{\phi^2}{2}) \right) \tag{38}$$

$$M'_V = V\left((t - z_{CA1})\phi + y_{CA1}(1-\frac{\phi^2}{2}) \right) \tag{39}$$

The internal moment for the triangular facet about XX' is therefore:

$$M'_{\text{int}} = M'_{Ty1} + M'_{CS} + M'_V \tag{40}$$

The external moment for the triangular facet about XX' is:

$$M'_{Ext} = \frac{prn_y l_y^2}{4}\left(t\phi + \frac{n_y l_y}{3}(1-\frac{\phi^2}{2}) \right) \tag{41}$$

The transverse shear force can be eliminated from these equations if Equations (40) and (41) are each multiplied by the factor $(-M_V / M'_V)$ and respectively added to Equations (35) and (36). The transverse equilibrium equation is then:

$$M_{Ext} - (M_V / M'_V)M'_{Ext} = (M_{Tx1} + M_{Tx2} + M_{CS} + M_{Cx2} + M_B) - (M_V / M'_V)(M'_{Ty1} + M'_{CS}) \tag{42}$$

This gives the enhanced value of the applied load for a case in which the steel temperature is kept constant:

<u>*x*-aligned mechanism</u>

For an *x*-aligned mechanism the equivalent equations for the triangular facet about YY' are:

$$M_{Tx1} = T_{x1}\left((x_{\lim,1x} + x_{T,1})\frac{\theta}{2} - t(1-\mu)(1-\frac{\theta^2}{2}) \right) \tag{43}$$

$$M_{CS} = (C\cos\gamma_x - S\sin\gamma_x)\left(-x_{CA1}\theta + (t - z_{CA1})(1-\frac{\theta^2}{2}) \right) \tag{44}$$

$$M_V = V\left((t - z_{CA1})\theta + x_{CA1}(1-\frac{\theta^2}{2}) \right) \tag{45}$$

$$M_B = \frac{B_T}{n_B}\left(\sum_{i=1}^{n_d}\left(\frac{il_y\tan\gamma_x}{(n_B+1)}\theta + \frac{h}{2}(1-\frac{\theta^2}{2}) \right) + \frac{n_{mid}}{2}\left(n_x l_y\theta + \frac{h}{2}(1-\frac{\theta^2}{2}) \right) \right) \tag{46}$$

The complete "internal" moment is then:

$$M_{\text{int}} = M_{Tx1} + M_{CS} + M_V + M_B \tag{47}$$

The external moment about YY' for this facet is:

$$M_{Ext} = \frac{p n_x l_y^2}{4}\left(t\theta + \frac{n_x l_y}{3}(1-\frac{\theta^2}{2}) \right) \tag{48}$$

For the trapezoidal facet the corresponding internal moment equations about XX' are:

$$M'_{Ty1} = T_{y1}\left((y_{\lim,1x} + y_{T,1})\frac{\phi}{2} - t(1-\mu)(1-\frac{\phi^2}{2}) \right) \tag{49}$$

$$M'_{Ty2} = T_{y1}\left(l_y \frac{\phi}{2} - t(1-\mu)(1-\frac{\phi^2}{2}) \right) \tag{50}$$

$$M'_{CS} = -(C\sin\gamma_y + S\cos\gamma_y)\left(y_{CA1}\phi - (t-z_{CA1})(1-\frac{\phi^2}{2}) \right) \tag{51}$$

$$M'_{Cy2} = -C_{y2}\left(l_y \frac{\phi}{2} - (t-\frac{z_2}{2})(1-\frac{\phi^2}{2}) \right) \tag{52}$$

$$M'_V = -V\left((t-z_{CA1})\phi + y_{CA1}(1-\frac{\phi^2}{2}) \right) \tag{53}$$

So that

$$M'_{\text{int}} = M'_{Ty1} + M'_{Ty2} + M'_{CS} + M'_{Cy2} + M'_V \tag{54}$$

The "external" moment about XX' is:

$$M'_{Ext} = \frac{p l_y^2}{2}\left((\frac{r}{2} - n_x)\left(t\phi + \frac{l_y}{4}(1-\frac{\phi^2}{2}) \right) + \frac{n_x}{2}\left(t\phi + \frac{l_y}{6}(1-\frac{\phi^2}{2}) \right) \right) \tag{55}$$

Again, the transverse shear force can be eliminated from these equations if Equations (54) and (55) are each multiplied by the factor $(-M_V / M'_V)$ and respectively added to Equations (47) and (48). The transverse equilibrium equation is then:

$$M_{Ext} - (M_V / M'_V)M'_{Ext} = (M_{Tx1} + M_{CS} + M_B) - (M_V / M'_V)(M'_{Ty1} + M'_{Ty2} + M'_{CS} + M'_{Cy2}) \tag{56}$$

Critical steel beam temperature

Since the yield strength of structural steel is assumed to degrade with temperature in the piecewise-linear linear manner defined by EN 1993-1-2 [16], it is not feasible to express the load capacity directly as a function of beam temperature and slab deflection. The enhanced value of load produced by these equations at any steel beam temperature and slab deflection may be greater or less than the pre-defined load intensity actually applied to the slab. It is easiest to increase the slab deflection in increments from zero; at each deflection the beam temperature is then iterated until the load capacity is within a

prescribed tolerance of the defined loading. In this process, the possibility of multiple solutions is avoided. Hence the enhancement of capacity of composite slab panels with unprotected steel beams by tensile membrane action can be defined as an enhancement of the critical beam temperature at a given applied load intensity by finite deflection. There will clearly be boundaries to the range of applied load within which this enhancement applies:

- At the lower end of applied loading, a non-composite version of the slab can carry the load, and so beam temperatures can rise above 1200°C.
- At the upper end, the composite slab carries the load without any reserve capacity at temperatures up to 400°C. Although it is possible that, at finite deflections, there may be sufficient enhancement to allow them to carry their loading at higher temperatures, this is impractical since such cases would not be acceptable under ambient-temperature ultimate limit state conditions.

3.6. Change of mechanism with deflection

For both types of mechanism there are 30 different possible combinations linking:

- The concrete stress-block shape, corresponding to:
  - Complete Figures 7(a, b): $z_2 > 0$;
  - Triangular Figures 7(c, d): $z_2 < 0, z_1 < t$;
  - Trapezoidal Figure 7(e): $z_2 < 0, z_1 > t$.
- The reinforcement fracture state, given by:
  - Intact or fractured bars crossing the central yield line;
  - Intact or partially fractured ("unzipping") bars in either direction crossing the diagonal yield lines.

Given the high ductility of structural steel members, especially at high temperatures, and the typically rather large spacing of shear studs, the possibility of tensile fracture of the downstand beams is not included in these scenarios. The 30 possible cases for the *x*-aligned mechanism are shown in Table 1, and the comparable cases for the *y*-aligned mechanism are shown in Table 2.

Compression block		Reinforcement mesh fracturing					
		None	Central *y* (all)	Diagonal *x*	Central *y* + diagonal *x*	Central *y* + diagonal *y*	Diagonal *x* and *y*
Full	above mesh	**a1x**	**a1x'**	**a1x***	**a1x'***	**a1x****	**a1x*****
	below mesh	**a2x**	**a2x'**	**a2x***	**a2x'***	**a2x****	**a2x*****
Triangular	above mesh	**b1x**	**b1x'**	**b1x***	**b1x'***	**b1x****	**b1x*****
	below mesh	**b2x**	**b2x'**	**b2x***	**b2x'***	**b2x****	**b2x*****
Trapezoidal		**cx**	**cx'**	**cx***	**cx'***	**cx****	**cx*****

Table 1: x-aligned cases: combinations of compression block configuration and rebar fracture.

Compression block		Reinforcement mesh fracturing					
		None	Central *x* (all)	Diagonal *y*	Central *x* + Diagonal *y*	Central x + Diagonal x	Diagonal *x* and *y*
Full	above mesh	**a1y**	**a1y'**	**a1y***	**a1y'***	**a1y****	**a1y*****
	below mesh	**a2y**	**a2y'**	**a2y***	**a2y'***	**a2y****	**a2y*****
Triangular	above mesh	**b1y**	**b1y'**	**b1y***	**b1y'***	**b1y****	**b1y*****
	below mesh	**b2y**	**b2y'**	**b2y***	**b2y'***	**b2y****	**b2y*****
Trapezoidal		**cy**	**cy'**	**cy***	**cy'***	**cy****	**cy*****

Table 2: y-aligned cases: combinations of compression block configuration and rebar fracture.

The process for constructing the in-plane equilibrium equations for each of the 30 cases for both mechanisms has been covered in detail in the previous paper, dealing with non-composite slabs without reference to elevated temperatures. For composite slabs in fire conditions, these equations are identical in all their terms except those representing the temperature-dependent forces in the unprotected downstand steel beams. As in the previous paper, it is convenient to present the equilibrium equations in dimensionless terms, and for this purpose the following parameters are defined:

$$\lambda_x = \frac{f_{px}}{f_c l},\ \lambda_y = \frac{f_{py}}{f_c l} \tag{57}$$

$$\beta = \frac{B_T}{f_c l^2} \tag{58}$$

$$\psi_1 = \frac{z_1}{l} \quad \text{and} \quad \psi_2 = \frac{z_2}{l} = \psi_1 - \frac{\theta n_x}{2} \tag{59}$$

$$\tau = \frac{t}{l} \tag{60}$$

$$\eta_x = \frac{\Delta_{lim,x}}{l} \quad \text{and} \quad \eta_y = \frac{\Delta_{lim,y}}{l} \tag{61}$$

In these terms, the in-plane equilibrium equations for the *x*-aligned cases defined in Table 1 are presented in Tables 3 to 5. The in-plane equilibrium equations for the *y*-aligned mechanisms defined in Table 2 are given in Tables 6 to 8.

4. APPLICATION OF THE MODEL

In Section 2 it was pointed out that the degree of orthotropy of a composite slab panel with unprotected downstand steel beams changes as the temperature of the steel beams rises. For a slab reinforced with isotropic mesh, and subject to a fixed loading intensity, at any particular downstand beam temperature the composite slab will have an optimum yield-line pattern which is associated with the lowest possible load capacity. Taking into account the strength of the downstand beams the net degree of orthotropy will be least at high temperatures and greatest at ambient temperature. The initial critical temperature, at which the load capacity intersects with the applied loading, therefore fixes the pattern of yield lines for the subsequent tensile membrane action as the beam temperature increases further and the slab deflection increases.

Case	$a\psi_1^2 + b\psi_1 + c = 0$					
	a	b		c		
a1x		$\left(\frac{1}{\sin\gamma\cos\gamma} + (r - 2n_x)\right)$		$-\frac{\theta n_x}{2}\left(\frac{1}{2\sin\gamma\cos\gamma} + (r - 2n_x)\right)$	$-\left(\lambda_x \frac{1}{2n_x} + \lambda_y r\right)$	$-\beta\frac{1}{2n_x}$
a1x'		$\left(\frac{1}{\sin\gamma\cos\gamma} + (r - 2n_x)\right)$		$-\frac{\theta n_x}{2}\left(\frac{1}{2\sin\gamma\cos\gamma} + (r - 2n_x)\right)$	$-\left(\lambda_x \frac{1}{2n_x} + 2\lambda_y n_x\right)$	$-\beta\frac{1}{2n_x}$
a1x*		$\left(\frac{1}{\sin\gamma\cos\gamma} + (r - 2n_x)\right)$	$-\lambda_x \frac{1}{\theta n_x^2}$	$-\frac{\theta n_x}{2}\left(\frac{1}{2\sin\gamma\cos\gamma} + (r - 2n_x)\right)$	$-\left(\lambda_x \frac{1}{\theta^2 n_x^2}(\eta_x - \theta\mu\tau) + \lambda_y r\right)$	$-\beta\frac{1}{2n_x}$
a1x'*		$\left(\frac{1}{\sin\gamma\cos\gamma} + (r - 2n_x)\right)$	$-\lambda_x \frac{1}{\theta n_x^2}$	$-\frac{\theta n_x}{2}\left(\frac{1}{2\sin\gamma\cos\gamma} + (r - 2n_x)\right)$	$-\left(\lambda_x \frac{1}{\theta^2 n_x^2}(\eta_x - \theta\mu\tau) + 2\lambda_y n_x\right)$	$-\beta\frac{1}{2n_x}$
a1x**		$\left(\frac{1}{\sin\gamma\cos\gamma} + (r - 2n_x)\right)$	$-\lambda_y \frac{4}{\theta}$	$-\frac{\theta n_x}{2}\left(\frac{1}{2\sin\gamma\cos\gamma} + (r - 2n_x)\right)$	$-\left(\lambda_x \frac{1}{2n_x} + 2\lambda_y \frac{1}{\theta^2 n_x}(\eta_y - 2n_x\mu\tau\theta)\right)$	$-\beta\frac{1}{2n_x}$
a1x***		$\left(\frac{1}{\sin\gamma\cos\gamma} + (r - 2n_x)\right)$	$-\lambda_x \frac{1}{\theta n_x^2} - \lambda_y \frac{4}{\theta}$	$-\frac{\theta n_x}{2}\left(\frac{1}{2\sin\gamma\cos\gamma} + (r - 2n_x)\right)$	$-\left(\lambda_x \frac{1}{\theta^2 n_x^2}(\eta_x - \theta\mu\tau) + 2\lambda_y \frac{1}{\theta^2 n_x}(\eta_y - 2n_x\mu\tau\theta)\right)$	$-\beta\frac{1}{2n_x}$
a2x		$\left(\frac{1}{\sin\gamma\cos\gamma} + (r - 2n_x)\right)$	$+\lambda_x \frac{1}{\theta n_x^2} + \lambda_y \frac{4}{\theta}$	$-\frac{\theta n_x}{2}\left(\frac{1}{2\sin\gamma\cos\gamma} + (r - 2n_x)\right)$	$-\left(\lambda_x(\frac{1}{2n_x} + \frac{\mu\tau}{\theta n_x^2}) + \lambda_y(r + \frac{4\mu\tau}{\theta})\right)$	$-\beta\frac{1}{2n_x}$
a2x'		$\left(\frac{1}{\sin\gamma\cos\gamma} + (r - 2n_x)\right)$	$+\lambda_x \frac{1}{\theta n_x^2} + \lambda_y \frac{4}{\theta}$	$-\frac{\theta n_x}{2}\left(\frac{1}{2\sin\gamma\cos\gamma} + (r - 2n_x)\right)$	$-\left(\lambda_x(\frac{1}{2n_x} + \frac{\mu\tau}{\theta n_x^2}) + \lambda_y(2n_x + \frac{4\mu\tau}{\theta})\right)$	$-\beta\frac{1}{2n_x}$
a2x*		$\left(\frac{1}{\sin\gamma\cos\gamma} + (r - 2n_x)\right)$	$+\lambda_y \frac{4}{\theta}$	$-\frac{\theta n_x}{2}\left(\frac{1}{2\sin\gamma\cos\gamma} + (r - 2n_x)\right)$	$-\left(\lambda_x \frac{\eta_x}{\theta^2 n_x^2} + \lambda_y(r + \frac{4\mu\tau}{\theta})\right)$	$-\beta\frac{1}{2n_x}$
a2x'*		$\left(\frac{1}{\sin\gamma\cos\gamma} + (r - 2n_x)\right)$	$+\lambda_y \frac{4}{\theta}$	$-\frac{\theta n_x}{2}\left(\frac{1}{2\sin\gamma\cos\gamma} + (r - 2n_x)\right)$	$-\left(\lambda_x \frac{\eta_x}{\theta^2 n_x^2} + \lambda_y(2n_x + \frac{4\mu\tau}{\theta})\right)$	$-\beta\frac{1}{2n_x}$
a2x**		$\left(\frac{1}{\sin\gamma\cos\gamma} + (r - 2n_x)\right)$	$+\lambda_x \frac{1}{\theta n_x^2}$	$-\frac{\theta n_x}{2}\left(\frac{1}{2\sin\gamma\cos\gamma} + (r - 2n_x)\right)$	$-\left(\lambda_x(\frac{1}{2n_x} + \frac{\mu\tau}{\theta n_x^2}) + \lambda_y \frac{2\eta_y}{\theta^2 n_x}\right)$	$-\beta\frac{1}{2n_x}$
a2x***		$\left(\frac{1}{\sin\gamma\cos\gamma} + (r - 2n_x)\right)$		$-\frac{\theta n_x}{2}\left(\frac{1}{2\sin\gamma\cos\gamma} + (r - 2n_x)\right)$	$-\left(\lambda_x \frac{\eta_x}{\theta^2 n_x^2} + \lambda_y \frac{2\eta_y}{\theta^2 n_x}\right)$	$-\beta\frac{1}{2n_x}$

Table 3: In-plane equilibrium equations for different possible x-aligned cases. Cases with concrete stress blocks on central and diagonal yield lines.

Case	$a\psi_1^2 + b\psi_1 + c = 0$			
	a	***b***	***c***	
b1x	$\frac{1}{\sin\gamma\cos\gamma}$		$-\left(\lambda_x\frac{\theta}{2}+\lambda_y r n_x\theta\right)$	$-\beta\frac{\theta}{2}$
b1x'	$\frac{1}{\sin\gamma\cos\gamma}$		$-\left(\lambda_x\frac{\theta}{2}+\lambda_y 2n_x^2\theta\right)$	$-\beta\frac{\theta}{2}$
b1x*	$\frac{1}{\sin\gamma\cos\gamma}$	$-\lambda_x\frac{1}{n_x}$	$-\left(\frac{\lambda_x}{n_x}\left(\frac{\eta_x}{\theta}-\mu\tau\right)+\lambda_y r n_x\theta\right)$	$-\beta\frac{\theta}{2}$
b1x'*	$\frac{1}{\sin\gamma\cos\gamma}$	$-\lambda_x\frac{1}{n_x}$	$-\left(\frac{\lambda_x}{n_x}\left(\frac{\eta_x}{\theta}-\mu\tau\right)+2\lambda_y n_x^2\theta\right)$	$-\beta\frac{\theta}{2}$
b1x**	$\frac{1}{\sin\gamma\cos\gamma}$	$-4\lambda_y n_x$	$-\left(\lambda_x\frac{\theta}{2}+\lambda_y(\frac{2\eta_y}{\theta}-4n_x\mu\tau)\right)$	$-\beta\frac{\theta}{2}$
b1x***	$\frac{1}{\sin\gamma\cos\gamma}$	$-\lambda_x\frac{1}{n_x}-4\lambda_y n_x$	$-\left(\frac{\lambda_x}{n_x}\left(\frac{\eta_x}{\theta}-\mu\tau\right)+\lambda_y\left(\frac{2\eta_y}{\theta}-4n_x\mu\tau\right)\right)$	$-\beta\frac{\theta}{2}$
b2x	$\frac{1}{\sin\gamma\cos\gamma}$	$+\lambda_x\frac{1}{n_x}+4\lambda_y n_x$	$-\left(\lambda_x\left(\frac{\theta}{2}+\frac{\mu\tau}{n_x}\right)+\lambda_y n_x(r\theta+4\mu\tau)\right)$	$-\beta\frac{\theta}{2}$
b2x'	$\frac{1}{\sin\gamma\cos\gamma}$	$+\lambda_x\frac{1}{n_x}+4\lambda_y n_x$	$-\left(\lambda_x\left(\frac{\theta}{2}+\frac{\mu\tau}{n_x}\right)+\lambda_y n_x(2n_x\theta+4\mu\tau)\right)$	$-\beta\frac{\theta}{2}$
b2x*	$\frac{1}{\sin\gamma\cos\gamma}$	$+4\lambda_y n_x$	$-\left(\lambda_x\frac{\eta_x}{n_x\theta}+\lambda_y n_x(r\theta+4\mu\tau)\right)$	$-\beta\frac{\theta}{2}$
b2x'*	$\frac{1}{\sin\gamma\cos\gamma}$	$+4\lambda_y n_x$	$-\left(\lambda_x\frac{\eta_x}{n_x\theta}+\lambda_y n_x(2n_x\theta+4\mu\tau)\right)$	$-\beta\frac{\theta}{2}$
b2x**	$\frac{1}{\sin\gamma\cos\gamma}$	$+\lambda_x\frac{1}{n_x}$	$-\left(\lambda_x\left(\frac{\theta}{2}+\frac{\mu\tau}{n_x}\right)+\lambda_y\frac{2\eta_y}{\theta}\right)$	$-\beta\frac{\theta}{2}$
b2x***	$\frac{1}{\sin\gamma\cos\gamma}$		$-\left(\lambda_x\frac{\eta_x}{n_x\theta}+\lambda_y\frac{2\eta_y}{\theta}\right)$	$-\beta\frac{\theta}{2}$

Table 4: In-plane equilibrium equations for different possible x-aligned cases. Cases with triangular concrete stress blocks on diagonal yield lines.

Case	$a\psi_1^2 + b\psi_1 + c = 0$					
	a	***b***		***c***		
cx		$\frac{2\tau}{\sin\gamma\cos\gamma}$	$+\frac{\lambda_x}{n_x}+4\lambda_y n_x$	$-\left(\frac{\tau^2}{\sin\gamma\cos\gamma}\right)$	$-\left(\lambda_x\left(\frac{\theta}{2}+\frac{\mu\tau}{n_x}\right)+\lambda_y n_x(r\theta+4\mu\tau)\right)$	$-\beta\frac{\theta}{2}$
cx'		$\frac{2\tau}{\sin\gamma\cos\gamma}$	$+\frac{\lambda_x}{n_x}+4\lambda_y n_x$	$-\left(\frac{\tau^2}{\sin\gamma\cos\gamma}\right)$	$-\left(\lambda_x\left(\frac{\theta}{2}+\frac{\mu\tau}{n_x}\right)+\lambda_y n_x(2n_x\theta+4\mu\tau)\right)$	$-\beta\frac{\theta}{2}$
cx*		$\frac{2\tau}{\sin\gamma\cos\gamma}$	$+4\lambda_y n_x$	$-\left(\frac{\tau^2}{\sin\gamma\cos\gamma}\right)$	$-\left(\lambda_x\frac{\eta_x}{n_x\theta}+\lambda_y n_x(r\theta+4\mu\tau)\right)$	$-\beta\frac{\theta}{2}$
cx'*		$\frac{2\tau}{\sin\gamma\cos\gamma}$	$+4\lambda_y n_x$	$-\left(\frac{\tau^2}{\sin\gamma\cos\gamma}\right)$	$-\left(\lambda_x\frac{\eta_x}{n_x\theta}+\lambda_y n_x(2n_x\theta+4\mu\tau)\right)$	$-\beta\frac{\theta}{2}$
cx**		$\frac{2\tau}{\sin\gamma\cos\gamma}$	$+\frac{\lambda_x}{n_x}$	$-\left(\frac{\tau^2}{\sin\gamma\cos\gamma}\right)$	$-\left(\lambda_x\left(\frac{\theta}{2}+\frac{\mu\tau}{n_x}\right)+\lambda_y\frac{2\eta_y}{\theta}\right)$	$-\beta\frac{\theta}{2}$
cx***		$\frac{2\tau}{\sin\gamma\cos\gamma}$		$-\left(\frac{\tau^2}{\sin\gamma\cos\gamma}\right)$	$-\left(\lambda_x\frac{\eta_x}{n_x\theta}+\lambda_y\frac{2\eta_y}{\theta}\right)$	$-\beta\frac{\theta}{2}$

Table 5: In-plane equilibrium equations for different possible x-aligned cases. Cases with trapezoidal concrete stress blocks on diagonal yield lines.

Case	$a\psi_1^2 + b\psi_1 + c = 0$					
	a	b		c		
a1y		$\left(\frac{r}{\sin\gamma\cos\gamma} + (1-2n_y)\right)$		$-\frac{\theta r}{4}\left(\frac{r}{2\sin\gamma\cos\gamma} + (1-2n_y)\right)$	$-\left(\lambda_x + \lambda_y\frac{r^2}{2n_y}\right)$	$-\beta$
a1y'		$\left(\frac{r}{\sin\gamma\cos\gamma} + (1-2n_y)\right)$		$-\frac{\theta r}{4}\left(\frac{r}{2\sin\gamma\cos\gamma} + (1-2n_y)\right)$	$-\left(2n_y\lambda_x + \lambda_y\frac{r^2}{2n_y}\right)$	$-\beta$
a1y*		$\left(\frac{r}{\sin\gamma\cos\gamma} + (1-2n_y)\right)$	$-\lambda_y\frac{2r}{\theta n_y}$	$-\frac{\theta r}{4}\left(\frac{r}{2\sin\gamma\cos\gamma} + (1-2n_y)\right)$	$-\left(\lambda_x + \lambda_y\frac{2}{\theta^2 n_y}(\eta_y n_y - \mu\tau r\theta)\right)$	$-\beta$
a1y'*		$\left(\frac{r}{\sin\gamma\cos\gamma} + (1-2n_y)\right)$	$-\lambda_y\frac{2r}{\theta n_y}$	$-\frac{\theta r}{4}\left(\frac{r}{2\sin\gamma\cos\gamma} + (1-2n_y)\right)$	$-\left(2n_y\lambda_x + \lambda_y\frac{2}{\theta^2 n_y}(2\eta_y n_y - \mu\tau r\theta)\right)$	$-\beta$
a1y**		$\left(\frac{r}{\sin\gamma\cos\gamma} + (1-2n_y)\right)$	$-\lambda_x\frac{2r}{\theta n_y}$	$-\frac{\theta r}{4}\left(\frac{r}{2\sin\gamma\cos\gamma} + (1-2n_y)\right)$	$-\left(\lambda_x\frac{2r}{\theta^2 n_y}(\eta_x - \mu\tau\theta) + \lambda_y\frac{r^2}{2n_y}\right)$	$-\beta$
a1y***		$\left(\frac{r}{\sin\gamma\cos\gamma} + (1-2n_y)\right)$	$-\lambda_x\frac{2r}{\theta n_y} - \lambda_y\frac{2r}{\theta n_y}$	$-\frac{\theta r}{4}\left(\frac{r}{2\sin\gamma\cos\gamma} + (1-2n_y)\right)$	$-\left(\lambda_x\frac{2r}{\theta^2 n_y}(\eta_x - \mu\tau\theta) + \lambda_y\frac{2}{\theta^2 n_y}(2\eta_y n_y - \mu\tau r\theta)\right)$	$-\beta$
a2y		$\left(\frac{r}{\sin\gamma\cos\gamma} + (1-2n_y)\right)$	$+\lambda_x\frac{8n_y}{\theta r} + \lambda_y\frac{2r}{\theta n_y}$	$-\frac{\theta r}{4}\left(\frac{r}{2\sin\gamma\cos\gamma} + (1-2n_y)\right)$	$-\left(\lambda_x(1+\frac{8n_y\mu\tau}{\theta r}) + \lambda_y\frac{r}{2n_y}(r+\frac{4\mu\tau}{\theta})\right)$	$-\beta$
a2y'		$\left(\frac{r}{\sin\gamma\cos\gamma} + (1-2n_y)\right)$	$+\lambda_x\frac{8n_y}{\theta r} + \lambda_y\frac{2r}{\theta n_y}$	$-\frac{\theta r}{4}\left(\frac{r}{2\sin\gamma\cos\gamma} + (1-2n_y)\right)$	$-\left(\lambda_x(2n_y+\frac{8n_y\mu\tau}{\theta r}) + \lambda_y\frac{r}{2n_y}(r+\frac{4\mu\tau}{\theta})\right)$	$-\beta$
a2y*		$\left(\frac{r}{\sin\gamma\cos\gamma} + (1-2n_y)\right)$	$+\lambda_x\frac{8n_y}{\theta r}$	$-\frac{\theta r}{4}\left(\frac{r}{2\sin\gamma\cos\gamma} + (1-2n_y)\right)$	$-\left(\lambda_x(1+\frac{8n_y\mu\tau}{\theta r}) + \lambda_y\frac{4\eta_y}{\theta^2}\right)$	$-\beta$
a2y'*		$\left(\frac{r}{\sin\gamma\cos\gamma} + (1-2n_y)\right)$	$+\lambda_x\frac{8n_y}{\theta r}$	$-\frac{\theta r}{4}\left(\frac{r}{2\sin\gamma\cos\gamma} + (1-2n_y)\right)$	$-\left(\lambda_x(2n_y+\frac{8n_y\mu\tau}{\theta r}) + \lambda_y\frac{4\eta_y}{\theta^2}\right)$	$-\beta$
a2y**		$\left(\frac{r}{\sin\gamma\cos\gamma} + (1-2n_y)\right)$	$+\lambda_y\frac{2r}{\theta n_y}$	$-\frac{\theta r}{4}\left(\frac{r}{2\sin\gamma\cos\gamma} + (1-2n_y)\right)$	$-\left(\lambda_x\frac{8\eta_x n_y}{\theta^2 r} + \lambda_y\frac{r}{2n_y}(r+\frac{4\mu\tau}{\theta})\right)$	$-\beta$
a2y***		$\left(\frac{r}{\sin\gamma\cos\gamma} + (1-2n_y)\right)$		$-\frac{\theta r}{4}\left(\frac{r}{2\sin\gamma\cos\gamma} + (1-2n_y)\right)$	$-\left(\lambda_x\frac{8\eta_x n_y}{\theta^2 r} + \lambda_y\frac{4\eta_y}{\theta^2}\right)$	$-\beta$

Table 6: In-plane equilibrium equations for different possible y-aligned cases. Cases with concrete stress blocks on central and diagonal yield lines.

Case	$a\psi_1^2 + b\psi_1 + c = 0$			
	a	***b***	***c***	
b1y	$\frac{1}{\sin\gamma\cos\gamma}$		$-\left(\lambda_x\frac{\theta}{2}+\lambda_y\frac{r^2\theta}{4n_y}\right)$	$-\beta\frac{\theta}{2}$
b1y'	$\frac{1}{\sin\gamma\cos\gamma}$		$-\left(\lambda_x n_y\theta+\lambda_y\frac{r^2\theta}{4n_y}\right)$	$-\beta\frac{\theta}{2}$
b1y*	$\frac{1}{\sin\gamma\cos\gamma}$	$-\lambda_y\frac{r}{n_y}$	$-\left(\lambda_x\frac{\theta}{2}+\lambda_y\left(\frac{2\eta_y}{\theta}-\frac{\mu\tau r}{n_y}\right)\right)$	$-\beta\frac{\theta}{2}$
b1y'*	$\frac{1}{\sin\gamma\cos\gamma}$	$-\lambda_y\frac{r}{n_y}$	$-\left(\lambda_x n_y\theta+\lambda_y\left(\frac{2\eta_y}{\theta}-\frac{\mu\tau r}{n_y}\right)\right)$	$-\beta\frac{\theta}{2}$
b1y**	$\frac{1}{\sin\gamma\cos\gamma}$	$-\lambda_x\frac{4n_y}{r}$	$-\left(\lambda_x\frac{4n_y}{r}\left(\frac{\eta_x}{\theta}-\mu\tau\right)+\lambda_y\frac{r^2\theta}{4n_y}\right)$	$-\beta\frac{\theta}{2}$
b1y***	$\frac{1}{\sin\gamma\cos\gamma}$	$-\lambda_x\frac{4n_y}{r}-\lambda_y\frac{r}{n_y}$	$-\left(\lambda_x\frac{4n_y}{r}\left(\frac{\eta_x}{\theta}-\mu\tau\right)+\lambda_y\left(\frac{2\eta_y}{\theta}-\frac{\mu\tau r}{n_y}\right)\right)$	$-\beta\frac{\theta}{2}$
b2y	$\frac{1}{\sin\gamma\cos\gamma}$	$+\lambda_x\frac{4n_y}{r}+\lambda_y\frac{r}{n_y}$	$-\left(\lambda_x\left(\frac{\theta}{2}+\frac{4\mu\tau n_y}{r}\right)+\lambda_y\frac{r}{4n_y}(r\theta+4\mu\tau)\right)$	$-\beta\frac{\theta}{2}$
b2y'	$\frac{1}{\sin\gamma\cos\gamma}$	$+\lambda_x\frac{4n_y}{r}+\lambda_y\frac{r}{n_y}$	$-\left(\lambda_x\left(n_y\theta+\frac{4\mu\tau n_y}{r}\right)+\lambda_y\frac{r}{4n_y}(r\theta+4\mu\tau)\right)$	$-\beta\frac{\theta}{2}$
b2y*	$\frac{1}{\sin\gamma\cos\gamma}$	$+\lambda_x\frac{4n_y}{r}$	$-\left(\lambda_x\left(\frac{\theta}{2}+\frac{4\mu\tau n_y}{r}\right)+\lambda_y\frac{2\eta_y}{\theta}\right)$	$-\beta\frac{\theta}{2}$
b2y'*	$\frac{1}{\sin\gamma\cos\gamma}$	$+\lambda_x\frac{4n_y}{r}$	$-\left(\lambda_x\left(n_y\theta+\frac{4\mu\tau n_y}{r}\right)+\lambda_y\frac{2\eta_y}{\theta}\right)$	$-\beta\frac{\theta}{2}$
b2y**	$\frac{1}{\sin\gamma\cos\gamma}$	$+\lambda_y\frac{r}{n_y}$	$-\left(\lambda_x\frac{4n_y\eta_x}{r\theta}+\lambda_y\frac{r}{4n_y}(r\theta+4\mu\tau)\right)$	$-\beta\frac{\theta}{2}$
b2y***	$\frac{1}{\sin\gamma\cos\gamma}$		$-\left(\lambda_x\frac{4n_y\eta_x}{r\theta}+\lambda_y\frac{2\eta_y}{\theta}\right)$	$-\beta\frac{\theta}{2}$

Table 6: In-plane equilibrium equations for different possible y-aligned cases. Cases with triangular concrete stress blocks on diagonal yield lines.

Case	$a\psi_1^2 + b\psi_1 + c = 0$					
	a	b		c		
cy		$\frac{2\tau}{\sin\gamma\cos\gamma}$	$+\lambda_x\frac{4n_y}{r}+\lambda_y\frac{r}{n_y}$	$-\left(\frac{\tau^2}{\sin\gamma\cos\gamma}\right)$	$-\left(\lambda_x\left(\frac{\theta}{2}+\frac{4\mu\tau n_y}{r}\right)+\lambda_y\frac{r}{4n_y}(r\theta+4\mu\tau)\right)$	$-\beta\frac{\theta}{2}$
cy'		$\frac{2\tau}{\sin\gamma\cos\gamma}$	$+\lambda_x\frac{4n_y}{r}+\lambda_y\frac{r}{n_y}$	$-\left(\frac{\tau^2}{\sin\gamma\cos\gamma}\right)$	$-\left(\lambda_x\left(\theta n_y+\frac{4\mu\tau n_y}{r}\right)+\lambda_y\frac{r}{4n_y}(r\theta+4\mu\tau)\right)$	$-\beta\frac{\theta}{2}$
cy*		$\frac{2\tau}{\sin\gamma\cos\gamma}$	$+\lambda_x\frac{4n_y}{r}$	$-\left(\frac{\tau^2}{\sin\gamma\cos\gamma}\right)$	$-\left(\lambda_x\left(\frac{\theta}{2}+\frac{4\mu\tau n_y}{r}\right)+\lambda_y\frac{2\eta_y}{\theta}\right)$	$-\beta\frac{\theta}{2}$
cy'*		$\frac{2\tau}{\sin\gamma\cos\gamma}$	$+\lambda_x\frac{4n_y}{r}$	$-\left(\frac{\tau^2}{\sin\gamma\cos\gamma}\right)$	$-\left(\lambda_x\left(\theta n_y+\frac{4\mu\tau n_y}{r}\right)+\lambda_y\frac{2\eta_y}{\theta}\right)$	$-\beta\frac{\theta}{2}$
cy**		$\frac{2\tau}{\sin\gamma\cos\gamma}$	$+\lambda_y\frac{r}{n_y}$	$-\left(\frac{\tau^2}{\sin\gamma\cos\gamma}\right)$	$-\left(\lambda_x\frac{4n_y\eta_x}{r\theta}+\lambda_y\frac{r}{4n_y}(r\theta+4\mu\tau)\right)$	$-\beta\frac{\theta}{2}$
cy***		$\frac{2\tau}{\sin\gamma\cos\gamma}$		$-\left(\frac{\tau^2}{\sin\gamma\cos\gamma}\right)$	$-\left(\lambda_x\frac{4n_y\eta_x}{r\theta}+\lambda_y\frac{2\eta_y}{\theta}\right)$	$-\beta\frac{\theta}{2}$

Table 7: In-plane equilibrium equations for different possible y-aligned cases. Cases with trapezoidal concrete stress blocks on diagonal yield lines.

4.1. Change of initial critical temperature with load intensity

The links between the applied load intensity, the critical yield line temperature and the geometry of the optimal yield line pattern are shown in Figures 9, 10 and 11 for four slabs of the same length (9.0m), depth (130 mm) and isotropic reinforcing mesh (142mm^2/m in either direction). The slabs all have downstand steel beams (UKB305x165x40 in S275) at 3m spacing, so that their ambient-temperature design capacity, considered as the conventional array of parallel composite beams, is the same in all cases. The 9m x 6m and 9m x 9m cases respectively represent the corner and internal slab panels used in the Cardington full-scale tests (Kirby [13]). The other cases, of 9m x 12m and 9m x 15m panels illustrate the effects on small-deflection yield-line behaviour of design decisions to remove fire protection from larger areas of floor slab.

It can be seen from Figure 9 that as the applied load changes the critical steel beam temperature changes between 400°C and 1200°C. For extremely low load intensities, the non-composite slab can carry the loading, and so steel temperatures are effectively irrelevant and can rise above the limit of 1200°C at which zero strength is assumed. At the other extreme, load intensities above the ambient-temperature capacity are unsustainable, even when the beams have lost none of their strength.

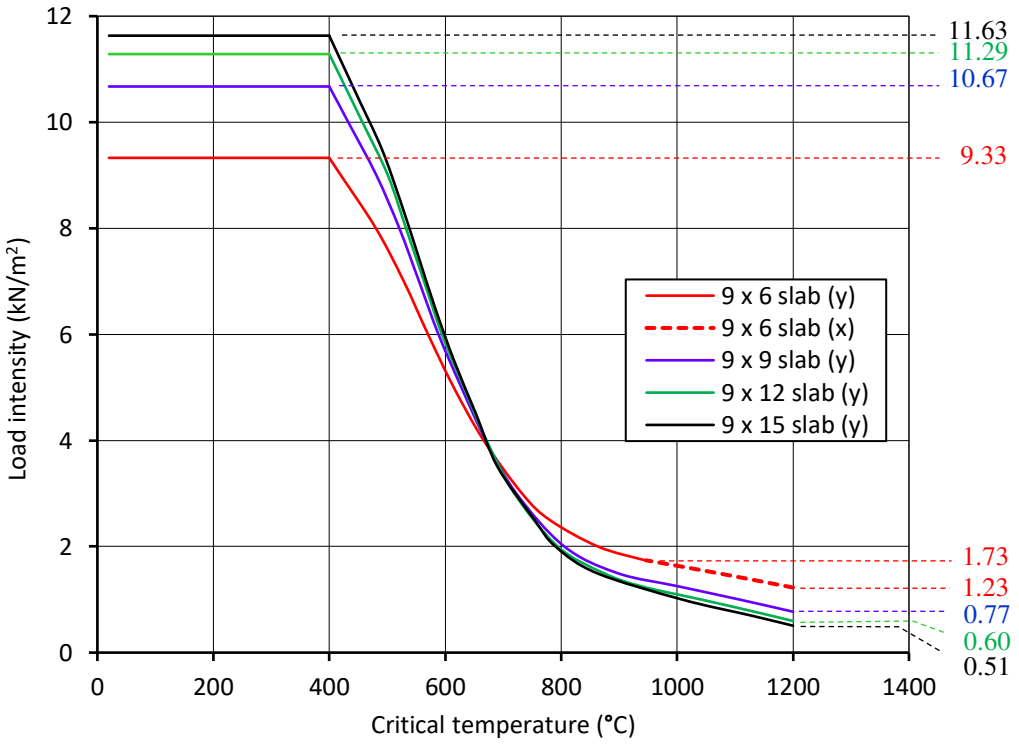

Figure 9: Change of small-deflection critical temperature of slabs of 9m length with downstand beams at 3m spacing, for different aspect ratios and variation of applied loading.

The geometry of the yield-line mechanisms associated with the initial critical temperatures is defined in Figures 9 and 10. Because of the inherent orthotropy of these composite slabs, the mechanisms are all *y*-aligned except for a small range of low load intensities for the 9m x 6m slab, which has only a

single longitudinal downstand beam, and has very high critical temperatures; this is most easily seen in Figure 9. Figure 10 shows the change of n_y for the yield-line mechanisms for each of the slab aspect ratios; in the x-aligned region of the 9m x 6m slab's curve n_y is represented by $\frac{r}{4n_x}$, which is the "virtual" n_y given by extrapolating a diagonal yield line to $rl/2$. In Figure 11 the absolute locations of the yield-line intersections are plotted against load intensity. This shows that, for any given load intensity, the distances of the yield-line intersections from the longitudinal edges of the slab are effectively constant.

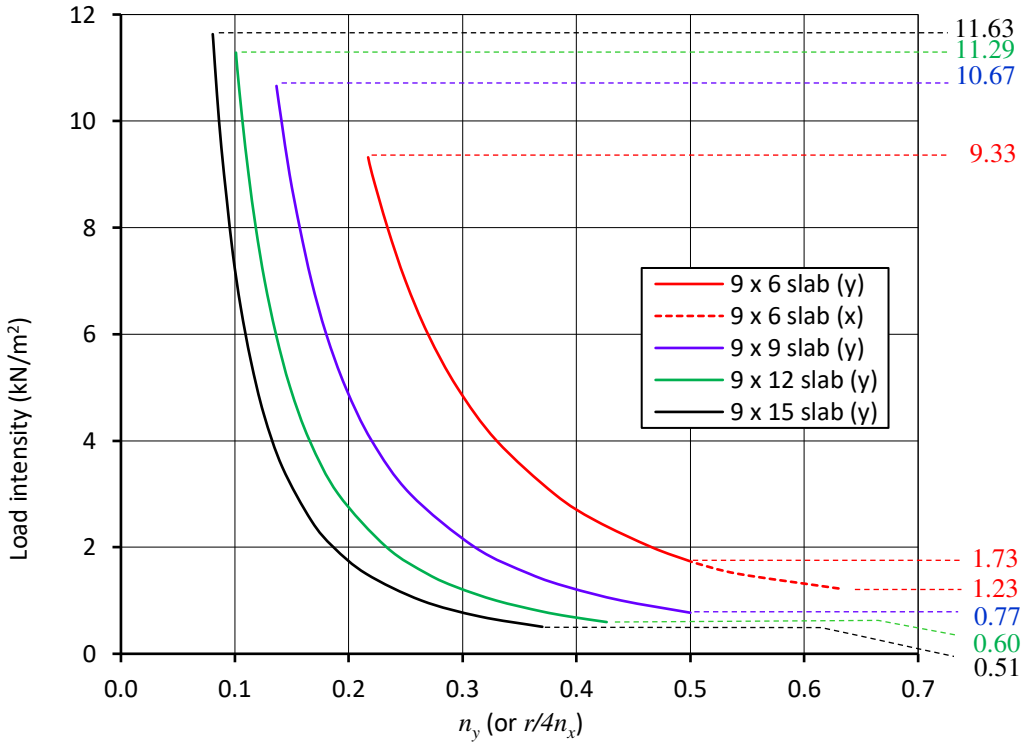

Figure 10: Change of small-deflection yield-line geometry parameter of slabs of 9m length with downstand beams at 3m spacing, for different aspect ratios and variation of applied loading.

This behaviour can be rationalized as an array of parallel composite beams behaving very similarly to their behaviour without continuity in the transverse direction. Each composite beam forms a mid-span plastic hinge, with small triangular areas of concrete as the only assistance to the load capacity deriving from the two-way support of the composite slab. The exception to this principle is where the applied loading is very low, and failure occurs at such high steel temperatures that the effect of the steel downstands almost vanishes; in this range, the yield-line behaviour mimics that of non-composite concrete slabs.

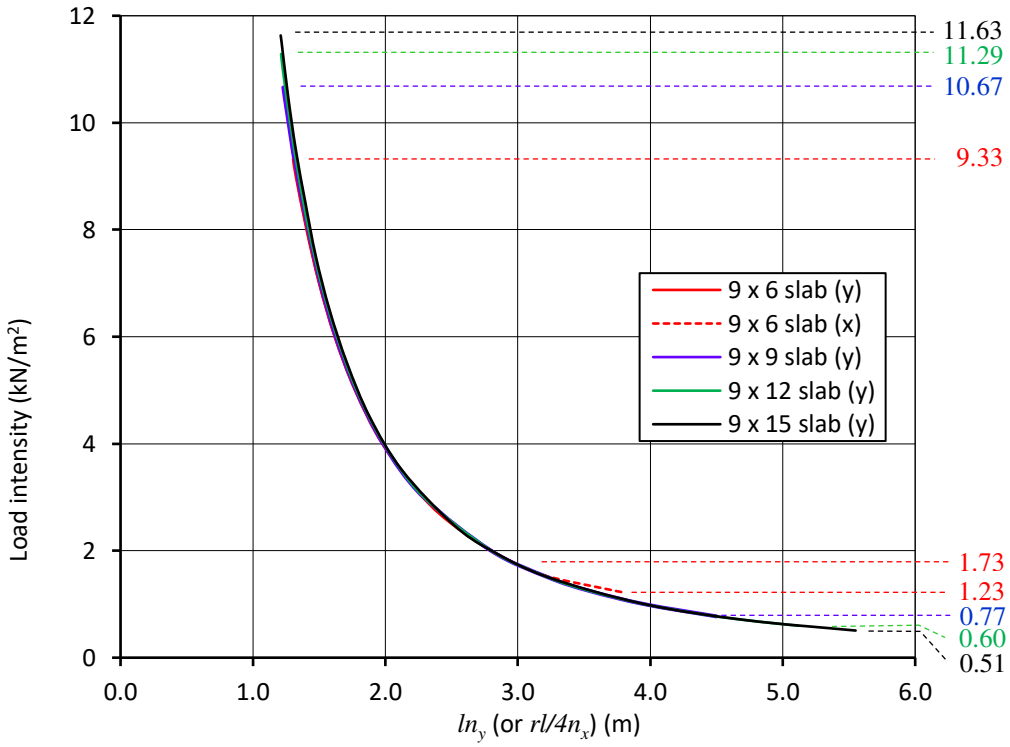

Figure 11: Change of small-deflection yield-line intersection coordinate of slabs a series of beam-strips of 9m length with downstand beams at 3m spacing, for different aspect ratios and variation of applied loading.

4.2. Enhancement of critical temperature by TMA: the effect of ductility

After a yield-line mechanism has formed at the initial critical temperature appropriate to the slab's loading intensity the slab continues to deflect as temperatures rise further. At various stages, the in-plane equilibrium phase changes, due to movement of the neutral axis depths z_1 and z_2, and due to fracture of rebar in either direction across yield lines. A typical example of these changes of phase as the slab deflection changes is shown in Figure 12.

This shows the change of critical beam temperature for one of the slabs used in the yield-line temperature studies above; a slab based on the Cardington "corner bay" panels, with overall dimensions 9m x 6m and A142 mesh of strength 500 MPa at an average effective depth of 38mm. The slab has an overall depth of 130mm and has concrete of strength 30 MPa. The single central secondary downstand beam is UKB305x165x40 of yield strength 275 MPa, and it is assumed that its temperature is uniform across its cross-section. Results for five fracture crack-widths (1mm, 1.5mm, 2mm, 2.5mm and 3mm) are shown. The surface loading intensity is 2kN/m^2; for this loading, the yield-line mechanism is *y*-aligned. The phase changes for the 1mm case are shown on Figure 12, and are annotated with the codes from Table 2:

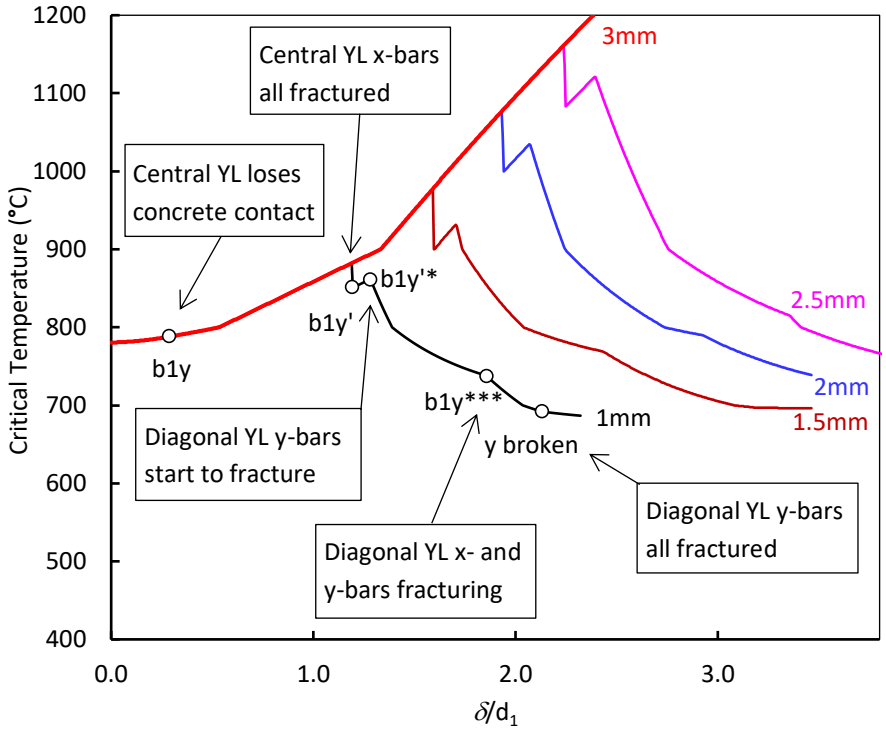

Figure 12: Enhancement sequence for 9m x 6m composite slab with central downstand beam, for different fracture crack-widths (1mm, 1.5mm, 2mm, 2.5mm, 3mm).

- **a1y:** The original state at infinitesimal deflection, shown graphically in Figures 7(a) and 7(b), in which concrete stress-blocks exist over the whole lengths of all yield lines, and no rebar has fractured.
- **b1y:** The state in which z_2 has become negative, indicating that concrete contact has ceased across the central yield line, and the concrete stress-blocks on the diagonal yield lines are triangular. There is still no fractured rebar.
- **b1y':** All the *x*-direction reinforcement crossing the central yield line fractures abruptly. After this has occurred the enhancement of critical temperature resumes.
- **b1y'*:** The *y*-direction reinforcement crossing the diagonal yield lines begins to fracture at the yield-line intersection, and then progressively "unzips" towards the slab corners as the deflection increases. This causes the critical temperature to decrease, and so the point gives the maximum enhancement at which this phase occurs.
- **b1y***:** The *x*-direction reinforcement crossing the diagonal yield lines begins to "unzip" from the intersection.

It can be seen that the "unzipping" of the *y*-direction reinforcement across the diagonal yield lines subsequently reaches the slab corner so that it is completely broken. At a later stage, the *x*-direction reinforcement also fractures completely. This does not imply complete collapse, because the downstand steel beam is still in place. The effect of allowing greater ductility can be seen by comparing the annotated curve with those for the higher fracture crack-widths. It can be seen that there is a common enhancement curve until the first reinforcement fracture occurs at a deflection, which varies with the prescribed fracture crack-width. The effect of greater pre-fracture ductility is to amplify the effect of

TMA to the extent that, at least for this particular loading case and slab definition, for 5mm fracture crack-width the temperature of the downstand beam can reach 1200°C without a de-stabilization of the equilibrium of the slab.

4.3. Enhancement of critical temperature by TMA: the effect of load intensity

Since enhancement of composite slab capacity is now defined, for any constant loading intensity and slab deflection, by the downstand beam temperature that can be sustained, it is appropriate to compare the temperature enhancement variations, which are given with deflection for various load levels. This is done in Figure 13 for slabs of three aspect ratios; 9m x6m, 9m x 9m and 9m x 12m. These are composed, respectively, of one, two and three identical parallel composite beams of span 9m and the details defined in Section 4.2 above. For each of these slab panels a number of load levels are used. The highest loading is just sustainable by the composite slab at temperatures up to 400°C, when the steel beam retains its full yield strength.

The lowest loading is almost at the level, which can be carried by the concrete slab alone, without any assistance from the steel downstand beams; this is equivalent to the beam temperature reaching 1200°C, at which the steel has no yield strength. Two collections of curves are shown for each aspect ratio, with fracture crack-widths of 1mm and 5mm. It should be noted that the yield-line mechanism is *y*-aligned for all load levels of the 9m x 9m and 9m x 12m slabs, and for all load levels above 1.73kN/m^2 for the 9m x 6m slab. The contrast between the collections of curves for low ductility (1mm fracture crack-width) and high ductility (5mm fracture crack-width) is quite clear. For all aspect ratios, it would be possible to take full advantage of TMA, if sufficient ductility is available in the form of an adequate fracture crack-width.

It must, of course, be remembered that it has been assumed in the development of this approach that the reinforcing mesh retains its full strength. For hot-rolled bars, this implies that the mesh temperature stays below 400°C, or for cold-drawn bars below 300°C [16]. There are two ways in which mesh can be heated; by conduction through the concrete slab and by radiation penetrating the narrow crack openings of the yield lines.

- In the case of conduction, for the slabs considered above, the temperature values given in EN 1992-1-2 Annex A [17], or those given in EN 1994-1-2 Annex D [18] may be used; these are linked solely to EN 1991-1-2 [19] standard fire exposure. The mesh location in the slab implies that for a typical composite slab cast on trapezoidal decking mesh temperatures stay below 300°C at 60 minutes and below 400°C at 90 minutes according to Eurocode 2 [16]. The corresponding times according to Eurocode 4 [18] are 90 minutes and 120 minutes respectively; for flat slabs of 130mm depth much longer fire resistance periods are implied.
- The case of radiation up the opening crack remains to be analysed in terms of the heat flux at the mesh level.

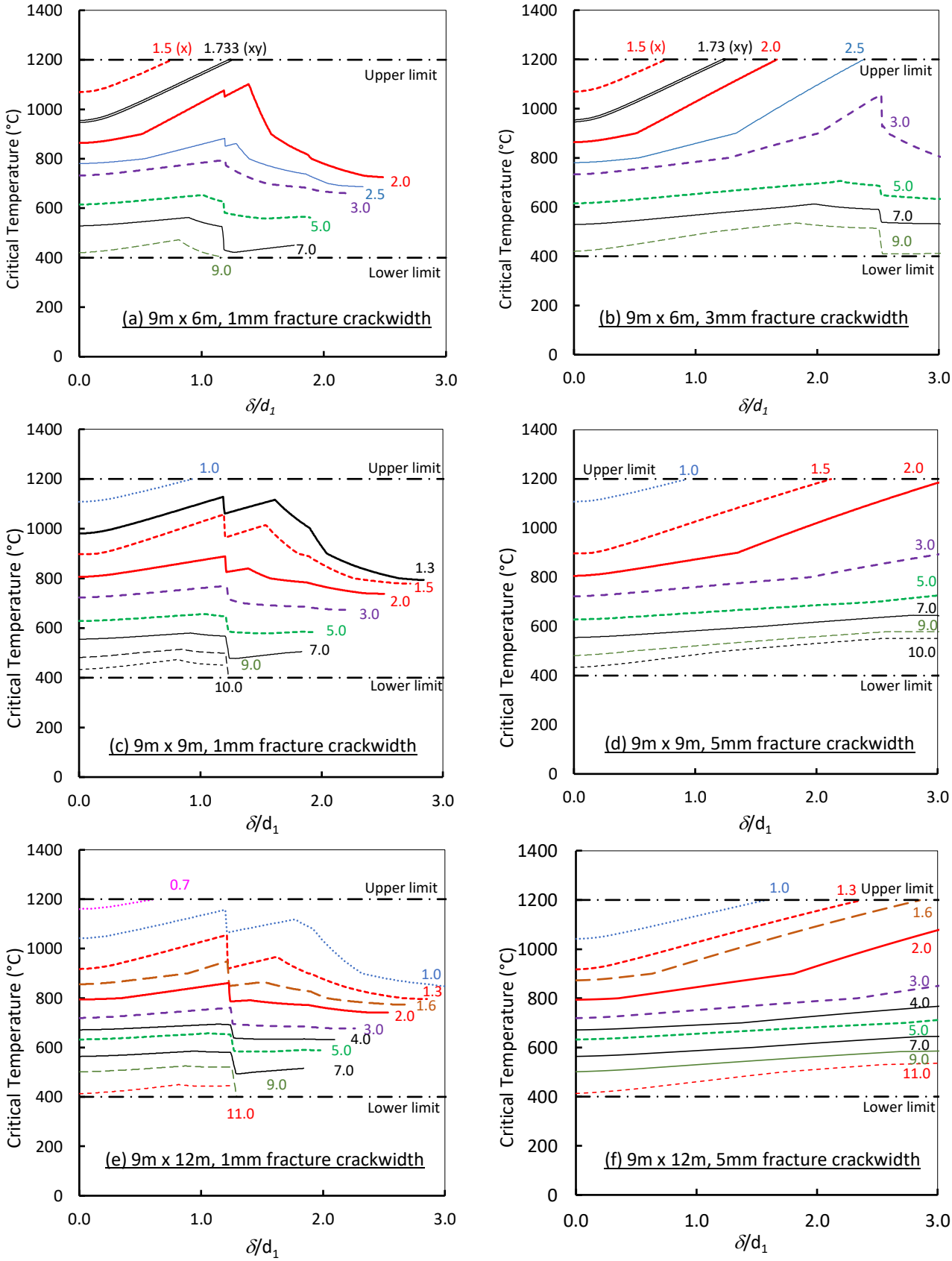

Figure 13: Downstand beam critical temperature enhancements with displacement for slabs of length 9m with different aspect ratios and fracture crack-widths. Slab load intensities are marked on individual curves.

5. IMPLICATIONS OF MESH BONDING FOR EFFECTIVE TENSILE MEMBRANE ACTION

In the preceding section, the ductility of the reinforcing mesh has been defined in terms of a fracture crack-width at the level of the mesh. At any location along a yield line the crack-width contains a length of bar which is under uniform stress; in the limiting (fracture) case this stress is at its ultimate value. Within the embedded length of bar the tensile stress must be lower than this at any point at which there is surface bond stress, and so fracture can only occur in the pulled-out length within the crack. Codified representations of the relationship between bond stress and bar slip are not helpful to attempts to find the fracture crack-width, because their focus is on maximizing the bond in reinforced concrete components and ensuring sufficient anchorage, rather than on quantifying slip. Work by Sezen and Setzler [20, 21] on concrete column ductility in the vicinity of beam connections under seismic shaking, which again considered bar pull-out at discrete cracks, produced a very simple model of bar slip which was verified against a series of 12 tests conducted by Sezen [22] and by Lynn *et al.* [23]. In this method, the stress-strain relationship for the rebar steel is assumed bilinear, with a shallow gradient between the yield and ultimate points. The bond stress within the embedded length from the crack-face is assumed to be locally constant, but to take one of two values, depending on whether the bar strain is "low" (elastic) or "high" (post-yield). This seems sensible, since little damage has been done to the concrete by the small bar strains in the elastic zone, whereas the much higher strains in the post-yield zone, and the large resulting slip movements of the bar surface deformations, cause real damage to the adjacent concrete. The model is illustrated in Figure 14.

The given bond stress values of $u_b = \sqrt{f_c}$ for the elastic zone and $u_b^{'} = 0.5\sqrt{f_c}$ for the post-yield zone are only numerically correct in SI units (MPa) and for deformed bars. Given the very simple nature of the distribution of bond stress the two parts of the development length l_d and $l_d^{'}$, and subsequently the crack-width can easily be calculated for a bar that has sufficient anchorage from its bond stresses and development lengths:

$$l_d = \frac{f_y d_b}{4u_b} \tag{62}$$

$$l_d^{'} = \frac{(f_s - f_y)d_b}{4u_b^{'}} \tag{63}$$

$$slip = \tfrac{1}{2}\left(\varepsilon_y l_d + (\varepsilon_s + \varepsilon_y) l_d^{'}\right) \tag{64}$$

In Figure 14 the general bar stress is denoted as f_b, bar yield stress is f_y and the ultimate stress is f_u; bar stress between f_y and f_u is denoted as f_s. When the crack-width is at the fracture level, then $f_s = f_u$ and $\varepsilon_s = \varepsilon_u$, the ultimate bar stress and strain values. In this state, the fracture crack-width is twice the

ultimate slip from a single crack-face. For welded orthogonal meshes the weld-points constitute physical "anchors" at regular spacing s_b, which can provide the reaction force balancing the tension in the bar at the weld-point. Each weld to the orthogonal bars has a strength which is guaranteed under Eurocode 2 to be at least 25% of the bar strength; if the bar tension at a weld-point exceeds the weld strength then the weld will fracture and the distance to the next weld-point will also become available for bond-slip. In this case, the pullout into the crack will increase abruptly when weld breakage occurs.

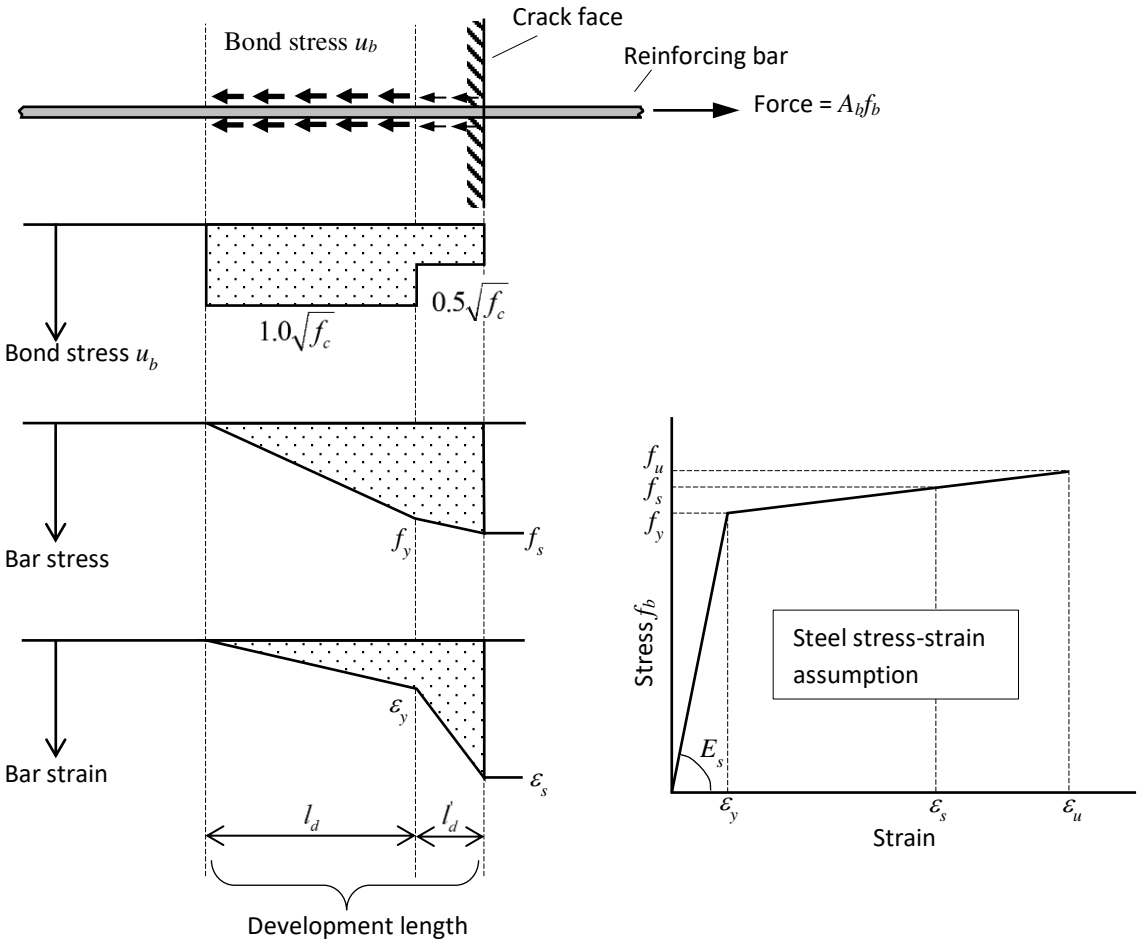

Figure 14: Reinforcement bar bond, stress and strain model, after Sezen and Setzler [20].

Some typical bar stress distributions are shown in Figure 14, in which the first transverse bar weld on one side of the crack is positioned at the average distance of $s_b/2$ from the crack-face, and subsequent welds are at the regular spacing s_b. For deformed bars which have very high bond stress it may be possible for the whole of the bar's fracture force to be carried by a development length which does not cross the first weld-point, as shown in Figure 15(a). Alternatively, the development length may reach this weld-point at bar fracture, but with insufficient bar stress to break the weld, as shown in Figure 15(b). In this case, the fracture crack-width is slightly lower than when the weld has broken and the additional anchorage force must be carried by the bond stress beyond the weld-point. For low-bond meshes, such as those composed of plain circular bars, a sequence similar to that shown in Figure 15(c)

can happen: even before bar yield the development length reaches the first weld-point, which subsequently breaks. Further welds may break before the necessary development length is reached to accumulate the bar fracture stress in the crack.

Both isotropic ("A" series) and orthotropic ("B" series) welded mesh fabrics are available for use in composite slabs. The fabric dimensions given in BS4483: 2005 [24] are shown in Table 9.

Mesh Type	Longitudinal Wires			Transverse Wires			
	Size (mm)	Pitch (mm)	Area (mm^2/m)	Size (mm)	Pitch (mm)	Area (mm^2/m)	Mass (kg/m^2)
A393	10	200	393	10	200	393	6.16
A252	8	200	252	8	200	252	3.95
A193	7	200	193	7	200	193	3.02
A142	6	200	142	6	200	142	2.22
B785	10	100	785	8	200	252	8.14
B503	8	100	503	8	200	252	5.93
B385	7	100	385	7	200	193	4.53
B283	6	100	283	7	200	193	3.7

Table 9: UK A and B series mesh types, from BS4483: 2005.

The isotropic meshes are most commonly used in composite slabs. In common with other types of steel reinforcement, three ductility classes are defined in BS4449: 2005 [25] and Eurocode 2 [16]; their strength and ductility characteristics are reproduced in Table 10.

Grade	BS4449				EN1992			Used for Case Studies			
		f_y (MPa)	f_u/f_y	ε_u	f_y (MPa)	f_u/f_y	ε_u	f_y (MPa)	f_u/f_y	f_u	ε_u
B500A	(<8mm)	500	1.02	1.0%	400-600	≥1.05	≥2.5%	490	1.02	500	1.0%
	(≥8mm)		1.05	2.5%				476	1.05	500	2.5%
B500B		500	1.08	5.0%		≥1.08	≥5.0%	463	1.08	500	5.0%
B500C		500	>1.15 ≤1.30	7.5%		≥1.15 ≤1.35	≥7.5%	435	1.15	500	7.5%

Table 10: Ductility Classes from BS4449:2005 and Eurocode 2, and the conservative assumptions which can be used for case studies.

The required development lengths and the slip from one crack-face at fracture, which is half of the fracture crack-width, in the absence of positive anchorage from transverse bar weld-points, can be calculated using Equations (50) to (52). If this required development length is pre-empted by a weld-point at which the bar force is insufficient to break the weld, then the actual development length is shortened, and the fracture crack-width is reduced. Since the calculation of fracture crack-width is based on a bilinear bar stress-strain assumption, albeit with a low post-yield stiffness, rather than the rigid-plastic assumption, which underpins the yield-line analysis and enhancement calculations, it is advisable to treat the fracture crack-width calculation in a way that underestimates it. In case studies, therefore, the nominal yield stress of reinforcing bars (500 MPa) is treated as the ultimate stress in the fracture crack-with calculation, and the f_u/f_y ratios specified in Table 10, bringing together the values

from BS4449 and Eurocode 2, are maintained. This effectively reduces the yield strength for each ductility class from the nominal value, as shown in Table 10.

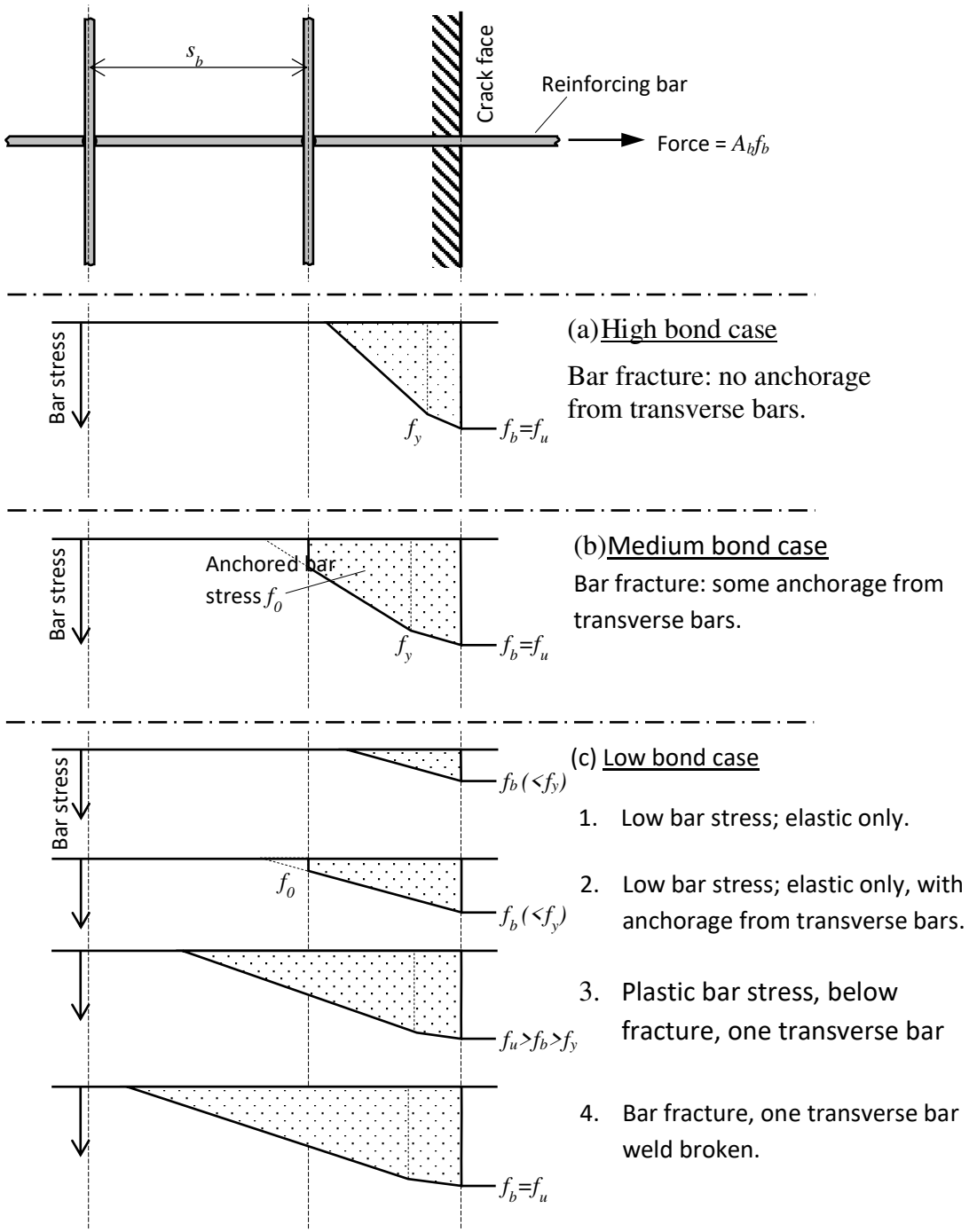

Figure 15: Bar tensile stress states: (a) development length less than orthogonal bar half-spacing at bar fracture; (b) some anchorage from transverse bar welds at bar fracture; (c) development sequence including weld breakage up to bar fracture.

The bond characteristics quoted by various researchers are summarized in Table 11.

		fib Model code [28]		Cashell [25]	Giroldo & Bailey [30]	Kankam [29]	Sezen & Setzler [19]		Used for these case studies	
Bar type		Poor bond	Good bond							
	f_c	u_b	u_b	u_b	u_b	u_b	u_b	u_b'	u_b	u_b'
Regular ribbed	30	4.0	5.9	2	4.5-5.5	6.8	5.5	2.7	5.5	2.7
Plain hot-rolled	30	0.8	1.6	1	1.3-2.0	1.3			1.6	0.8

Table 11: Bond strengths (MPa) from different research studies for different rebar types.

The elastic-zone and plastic-zone bond stresses for deformed bars are conveniently defined using the Sezen [20] model as having magnitudes in SI units of $u_b = \sqrt{f_c}$ and $u_b' = 0.5\sqrt{f_c}$ respectively. For plain undeformed bars, less consistent results are available; Cashell *et al.* [26, 27] performed a large number of pull-out and flexural tests on reinforced concrete specimens. Although it was acknowledged that a two-zone bond stress-slip model is justifiable, theirs was a single-zone approach with an assumed constant value of bond stress lying between those for the elastic and plastic zones. Although a range of experimental values was found, the very general recommendation for slab design purposes was to use 2 MPa and 1 MPa as single bond strengths for deformed and plain bars respectively, on the basis that deflections at failure would be lower for higher bond stress values. Herraiz and Vogel [28], in a study on tensile membrane action modelling, adopted the *fib* Model Code [29] expressions for single average bond stress. For "good bond conditions", these expressions are $5.6\left(\frac{f_{cm}}{25}\right)^{0.25}$ for hot-rolled deformed bars, and $0.3\sqrt{f_{cm}}$ for hot-rolled plain bars, giving 5.86 MPa and 1.64 MPa respectively for concrete of strength 30 MPa. Kankam [30] tested 30 specimens, albeit with bar diameters larger than those used in composite slabs, and quoted single average bond strengths of 6.8 MPa and 1.3 MPa from tests on deformed and plain bars respectively. Giroldo and Bailey [31] tested both deformed and plain bars at various temperatures, but presented the results only in terms of a single experimental bond stress-slip curve for each bar type, diameter and temperature. Observation of these curves suggests that their ambient-temperature tests for deformed bars indicate a single average bond stress in the region of 4.5 MPa for 6mm bars and 5.5 MPa for 8mm bars. The ambient-temperature curves for plain bars indicate a single average bond stress (more indicative of u_b' than u_b) beyond an initial peak caused by fracturing of a weld anchorage, in the region of 1.3 MPa for 6mm bars and 2 MPa for 8mm bars. These studies give some support to the Sezen model for deformed bars. On the basis of the average bond stress results for plain bars from these studies, the apparent values for plain bars are between 20% and 40% of those for deformed bars; for the purpose of these studies the values of the two bond stresses are set at the mean of these: $u_b = 0.3\sqrt{f_c}$ and $u_b' = 0.15\sqrt{f_c}$.

As has been stated above, the unbalanced bar stress at which welds to transverse bars break is guaranteed to be at least 25% of the bar strength; for these analyses the weld strength is assumed to be 50% of the bar strength. The effect of this as the stress f_s is increased is illustrated in Figure 16 in terms of the anchorage stress f_0 at the end of the development length and the development length over which bond slip happens, for A252 meshes (200mm x 200mm spacing) composed of 8mm plain bars of ductility classes B and C. The effect of successive breakage of the bars 100mm and 300mm from the crack-face can be seen for both ductility classes, with the eventual, natural development length stopping just short of the weld at 500mm from the crack-face. For deformed meshes of the same type the much greater bond strength reduces the development lengths considerably; it can be seen from Table 12 that for A142 deformed mesh no welds break, and for A252 only the first weld breaks. The effect of bar ductility and bond strength on the fracture crack-widths can also clearly be seen from this table.

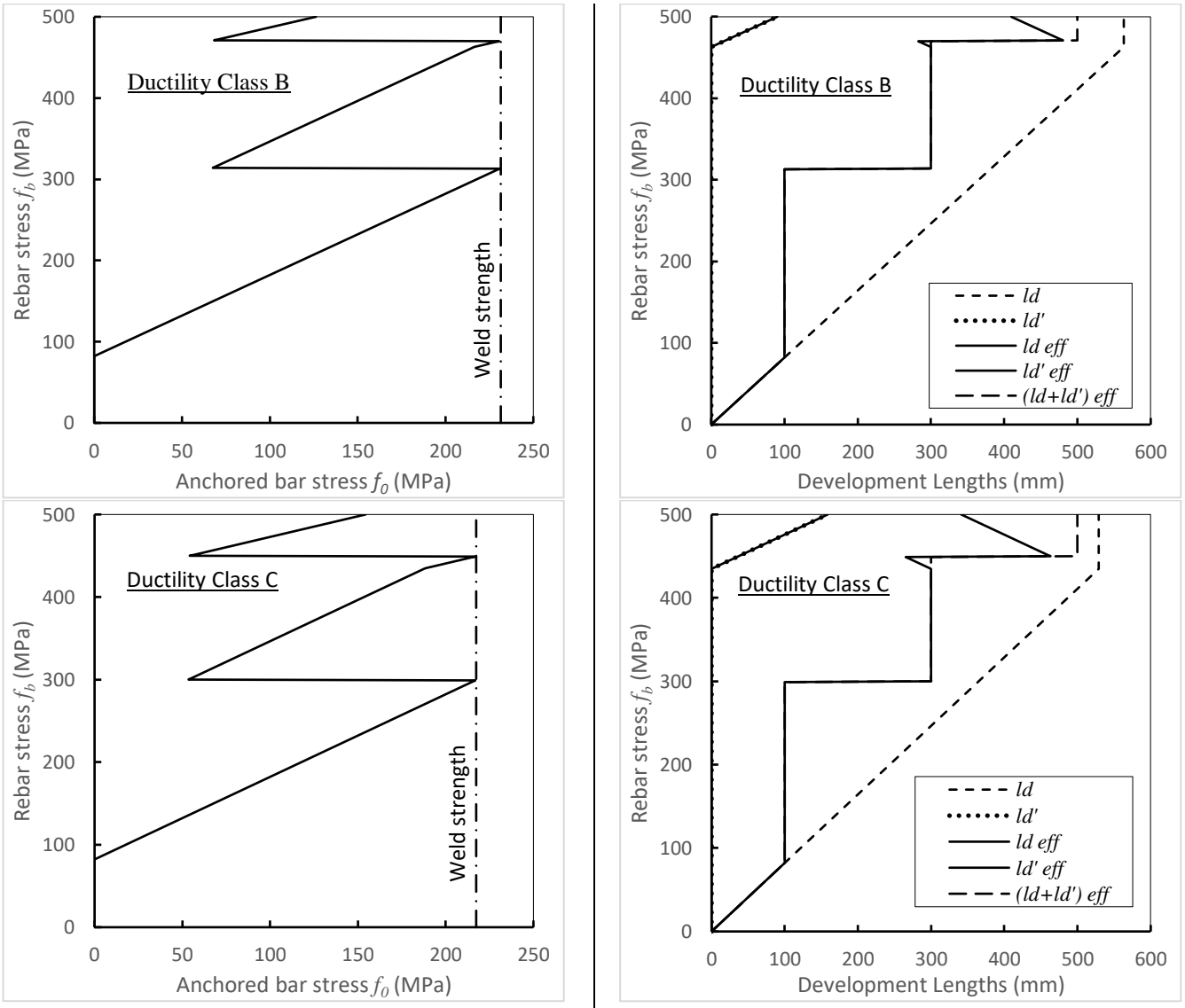

(a) (b)

Figure 16: Change with bar stress f_s outside the concrete (in the yield-line crack) of: (a) the bar stress f_0 which is anchored by a weld; (b) the development lengths which mobilize bond, including anchorage at welds. All curves are for 8mm plain bars.

ID	Bar diameter	Deformed / Smooth	Ductility class	Strengths		Ultimate strain	Natural Anchorage lengths			Weld fractures				Fracture crack-width	
				f_y	f_u	ε_u	l_d	l_d'	(l_d+l_d')	1st	2nd	3rd	Actual development length	Anchored	Natural
	(mm)			(Mpa)	(Mpa)		(mm)	(mm)	(mm)	(100mm)	(300mm)	(500mm)	(mm)	(mm)	(mm)
A142	6	Deformed	B	463	500	0.050	126.8	20.3	147.1	N	N	N	100.0	1.30	
			C	463	500	0.075	119.1	35.7	154.8	N	N	N	100.0	2.95	
		Smooth	B	463	500	0.100	422.6	67.6	490.2	Y	N	N	300.0	7.65	
			C	463	500	0.120	396.9	119.1	516.0	Y	Y	N	500.0	15.36	
A252	8	Deformed	B	435	500	0.050	169.1	27.0	196.1	Y	N	N	196.1		1.78
			C	435	500	0.075	158.8	47.6	206.4	Y	N	N	206.4		4.00
		Smooth	B	435	500	0.100	563.5	90.2	653.7	Y	Y	N	500.0	10.36	
			C	435	500	0.120	529.2	158.8	688.0	Y	Y	N	500.0	20.34	

Table 12: Fracture crack-widths for the A142 and A252 meshes of ductility classes B and C used in case studies.

Case studies, which once again feature composite slabs comprising parallel composite beams of the specification used for secondary beams in the Cardington full-scale building fire tests, as defined in Section 4.2, were conducted for panels of three aspect ratios (1.5, 1.0 and 0.75). A single load level of 5.36 kN/m^2, the Fire Limit State design load intensity appropriate to the design assumptions for the Cardington building, is used for these studies. As in the previous analyses, the nominal strengths for the concrete and the steel section were used, rather than the higher strengths obtained from materials testing during the Cardington programme. The resulting critical temperatures are plotted against slab deflection in Figure 17 for the three slab aspect ratios and the mesh ductility classes B and C. In general terms it is obvious that the enhancement of peak steel temperature with deflection is highly dependent on the fracture crack-width. It is also clear that high-aspect-ratio panels (with the composite beams spanning in the longer direction) are the most sensitive to this aspect of ductility.

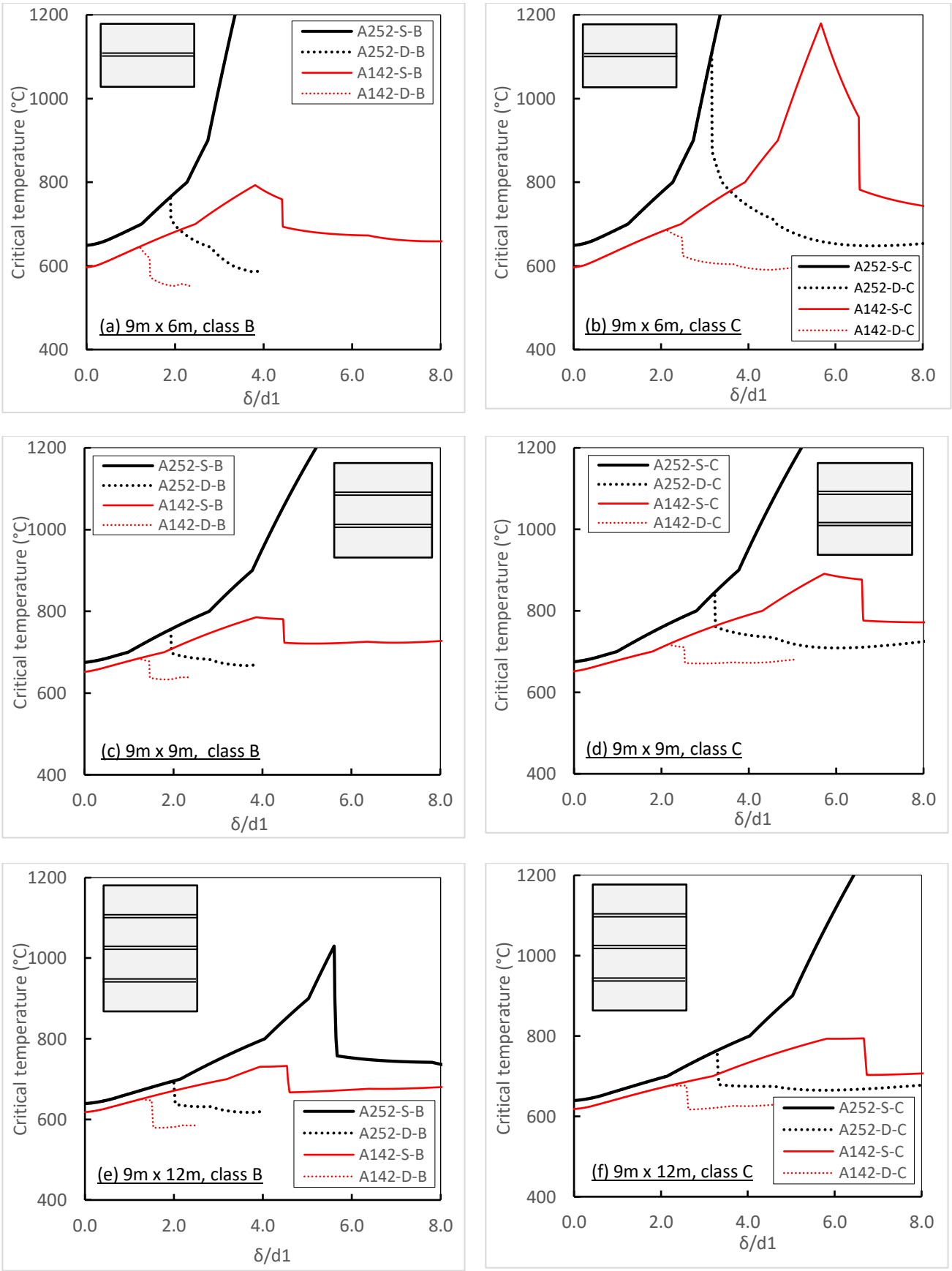

Figure 17: Downstand beam critical temperature enhancement factors with displacement for slabs of length 9m with different aspect ratios for A142 and A252 meshes of deformed and smooth bars. FLS design load of 5.36kN/m^2 in all cases.

6. CONCLUSION

The approach outlined in this paper is based on the assumption that an optimum rigid-plastic yield-line pattern is valid for a composite slab with very light reinforcing mesh. Subject to this assumption, the approach enables the large-deflection load capacity to be calculated given any beam yield strength, which is equivalent to calculating the enhancement of limiting beam temperature for a case in which the applied load remains constant. In terms of ISO834 standard fire exposure, this implies that the enhancement can be directly measured in terms of fire resistance time, requiring only a calculation of heat transfer to the unprotected downstand steel beams. This is also true for other exposures such as parametric fires.

6.1. Differences from previous approaches

The most notable current analytical approach to TMA of composite floors is that developed by Bailey *et al*. [31-36], based on the doctoral research of Hayes [9]. This assumes that the geometry of the yield-line pattern is that of the non-composite concrete slab, which has been shown earlier to be incorrect for composite panels. For non-trivial deflections a distribution of membrane force per unit length is assumed, which is not capable of changing with deflection and which implicitly assumes that concrete stress blocks always exist over the whole of all yield lines, as well as an assumed central tension crack, which represents the failure condition. The equilibrium of the membrane forces and plastic moments on each slab facet then produce independent enhancements of the yield-line capacity, which are then combined to give a weighted average enhancement. This enhanced load capacity of the concrete slab at any deflection is then added to the high-temperature load capacity of the array of composite beams of which form the panel. This is clearly illogical in a nonlinear system. The deflection at the occurrence of the final tension crack is predicted by superposing deflections due to thermal bowing of a simply supported strip of slab under a linearized temperature distribution onto the "catenary" deflection for a fixed-ended strip under half the ambient-temperature yield strain of the reinforcement. This superposition of deflections of systems with different boundary conditions is not legitimate, but the total is used as the limiting deflection for the capacity enhancement.

In the same context, the experimental evidence for the appearance of a purely-tensile short-span crack as a failure state in composite (as opposed to lightly-reinforced concrete) slab panels in fire seems rather slight. Even the post-test observation of a closed mid-span crack across the upper surface of a panel at Cardington [32] seems likely to reflect the compression zone of the y-aligned central yield line which would occur in this case, after reduction of the deflection due to cooling. There was certainly no evidence that this crack had opened across the full depth of the slab during the fire. Clearly, there is a possibility that tensile through-depth cracks may appear at extremely high steel temperatures (and therefore for very low load-levels), when the downstand beams have lost nearly all of their strength, across the triangular or trapezoidal facets rotating about the slab edges parallel to these downstand beams. This eventuality clearly needs to be investigated in extensions of the work. In terms of

compartment integrity failure, however, the loss of concrete contact across the central yield line, which happens relatively early, provides a more likely route for the fire to breach the compartmentation.

Although this method and the one presented here are both based on yield-line theory, the method described above has several defects. It uses a non-optimal yield line pattern for a composite slab, does not consider the kinematics of the system of slab facets so that its assumed membrane force pattern does not change with deflection, uses a weighted average capacity enhancement whose origin is unexplained and uses an impermissible superposition of deflections as its indicator of the failure deflection. These flaws suggest that the method is unsatisfactory to predict the failure states of general design cases.

The more recent approach of Omer *et al.* [37, 38] for the strength of lightly reinforced concrete slabs is in several ways similar to that presented here. Equilibrium is based on the kinematics of the facets of the optimal yield-line mechanism of the slab, although the concrete forces across yield lines are concentrated at discrete points of contact rather than creating stress blocks whose shape changes with deflection; this is very similar in principle to an earlier simplified approach [39] adopted by the first author. A bond-slip model is adopted, and failure is defined by fracture of the reinforcement at the assumed full-depth short-span crack, either at mid-span or at the yield-line intersection. However, it does not consider the effect of reinforcement fracture within the yield lines themselves. The method includes a steel constitutive model with both yield and ultimate strengths, and uses a virtual work solution process to establish equilibrium at finite deflections. Omer includes a process, based on dividing the slab into a series of beam-strips, for including the effect of thermal curvature of the concrete facets. This is discussed in the following section.

6.2. Possible effects of heating of the panel

It is true that the temperatures of the concrete slab, or of the mesh within it, have not been considered so far. It has been shown in Section 4.3 that reduction of the strength of the mesh because of direct conduction of heat to it through the concrete is of minor importance for the typical composite arrangement considered. In fact, the effect of differential expansion of bars and their surrounding concrete may have the beneficial effect of reducing bond, and thus increasing the fracture crack-widths. Both effects of this heating mechanism clearly need to be investigated further. Heating of the bars crossing opening yield-line cracks by direct radiation and convection from the fire below is potentially much more dangerous, because this creates a “hot spot”, which does not increase the bar slip from the crack-faces, but does locally weaken the steel within the crack. An investigation of this heat transfer within an opening crack in which the steel is exposed is also clearly needed.

Another possible effect due to the temperature distribution through the depth of the concrete slab at any time of fire exposure has been neglected in the development so far. The effect of differential heating, and therefore of differential thermal expansion, through the depth of the concrete facets has not been included. In equilibrating the stresses caused by this differential expansion a “thermal bowing” of the

composite panel is caused. A further bowing effect on the facets can be caused by the thermal expansion of the downstand beams, restrained by the shear connection to the underside of the concrete slab, which creates bending moments along the lines of the beams. This extra deflection will certainly increase the lever-arms of the internal forces acting on yield lines in the lateral load capacity calculation given in Section 3.5, and it can therefore be anticipated that the critical steel beam temperatures will increase across the range of additional deflection. This analysis does not attempt to *predict* the deflection of a panel with either temperature or fire exposure time, but simply considers its equilibrium under plastic limit state conditions, and so the thermal expansion of the downstand steel beams across yield lines need not be included. The challenge is therefore to represent adequately the effect of thermal bowing of the facets within the yield-line context. It could be considered that, at the time of initial formation of the yield-line mechanism, the panel has an initial deflection of a certain magnitude. This involves assigning a value to this initial displacement of the arrangement of flat facets, which represents properly the deflection caused by their thermal curvatures. In doing this a linearized temperature distribution, as has been used by Omer *et al.* [37, 38] in the only study which has so far attempted to account for thermal curvature, should be adequate at least to establish the essential behaviour. Omer's approach was also to represent the thermal expansion effects as free net expansion and curvatures of beam-strips across the slab facets of plain concrete slabs, tapering to zero curvature at the supported edges, although he states that the separate nature of the curves in adjacent facets causes some inaccuracy in the early stages of heating. A further approach, which seems appropriate, might be to match the initial yield-line deflection of the faceted model with that of the thermally curved slab using its first Fourier coefficient. Different representations of the thermal curvature effects will be tested in extensions of this work.

6.3. Implications of the work

The main spur to developing the approach presented in this paper was a desire to understand the basic mechanics of, and the more important influences on, the large-deflection behaviour of composite slabs at high temperatures. Although the yield-line method is in itself a simplification, its assumption of discrete hinges separating flat facets is at its most justifiable for slabs with low percentages of reinforcement, for which cracking tends to localize. It was considered important to represent the kinematics, together with the equilibrium, of the facets correctly within the yield-line context, and to be able to show the effect of reinforcement fracture across yield lines. For composite panels the heating of the steel downstand beams clearly causes them to weaken progressively, and so it seems logical to express the enhanced resistance in terms of the temperatures of these beams. Several issues need to be considered in further development of the work. Some of these have been discussed above. There is also a considerable need for carefully conducted experiments, either full-scale or model-scale, on composite panels under increasing temperatures, both for validation and in order to reveal aspects of their behaviour, which may have been omitted. It was not considered that experimental results exist at present, which would justify a comparison with this method. In order to compare the method with numerical analysis a finite element model, which includes prediction of discrete concrete cracks, a

reinforcement bond model which allows bars to pull out from the crack-face, and fracture of individual bars, is needed. This is feasible, but is currently at the leading edge of finite element modelling.

In design terms, it has been seen that the main factor in successful utilization of tensile membrane action in enhancing the load capacity of composite floors in fire, is ductility. This ductility is characterized by the fracture crack-width, which is controlled by the inherent ductility of the bar material and the slip which it can experience from each crack-face. In contrast to the normal principle of reinforced concrete design, it is advantageous to minimize the bond strength, at least in the areas where yield lines form. For welded meshes composed of plain bars the ductility provided by the weld spacing alone may be sufficient to produce an adequate fracture crack-width, and if the welds are weak compared to the tensile strength of the bars then fracture of the first weld on each side of the crack will further increase the ductility of the mechanism. For normal slab, bending resistance the presence of unbroken welds at working loads will ensure that plain reinforcing mesh is still involved, although its stress locally may be marginally lower than it would be with perfect continuous bond. Class C mesh is generally considered an expensive choice, but may be advantageous in some cases; an alternative, illustrated in Figure 16, is to use mesh with greater cross-sectional area (say A252 in place of A142).

The key aspects of tensile membrane action, considered as a structural fire engineering strategy for lightly reinforced composite slabs, have been illustrated in this paper, subject to very standard assumptions. Although some questions remain to be addressed in further work, the principles seem logical for cases where discrete yield lines form because of the localization of cracking associated with small percentages of reinforcement.

REFERENCES

[1] Johansen, K.W., *"Brudlinieteorier"*, Copenhagen 1943. (English translation *"Yield-Line Theory"*, Cement and Concrete Association, London, 1962).

[2] Hognestad, E., "Yield-line theory for the ultimate flexural strength of reinforced concrete slabs", *ACI Journal*, **49**, March 1953.

[3] Wood, R.H., *"Plastic and elastic design of slabs and plates, with particular reference to reinforced concrete floor slabs"*, Thames and Hudson, London, 1961.

[4] Park, R., "Tensile membrane behaviour of uniformly loaded rectangular reinforced concrete slabs with fully restrained edges", *Magazine of Concrete Research*, **16** (46), (1964) pp 39-44.

[5] Park R., "Ultimate strength of rectangular concrete slabs under short-term uniform loading with edges restrained against lateral movement", *Proc. Institution of Civil Engineers*, **28**, (1964) pp 125-150.

[6] Sawczuk, A. and Winnicki, L., "Plastic behavior of simply supported reinforced concrete plates at moderately large deflections", *Int. J. Solids Structures*, **1**, (1965) pp 97-111.

[7] Kemp, K.O., "Yield of a square reinforced concrete slab on simple supports, allowing for membrane forces", *The Structural Engineer*, **45** (7), (1967) pp 235-240.

[8] Hayes, B., "Allowing for membrane action in the plastic analysis of rectangular reinforced concrete slabs", *Magazine of Concrete Research*, **20** (65), (1968) pp 205-212.

[9] Hayes, B., *"A study of the design of reinforced concrete slab structures"*, PhD thesis, University of Manchester, 1968, 398 pp.

[10] Brotchie, J.F. and Holley, M.J., *"Membrane action in slabs: cracking, deflection and ultimate load of concrete slab systems"*, Publication SP-30, American Concrete Institute, Detroit, Paper 30-16, (1971) pp 345-377.

[11] Park, R. and Gamble, W., *"Reinforced concrete slabs"*, Wiley, London, 2000.

[12] Burgess, I.W., "Yield-Line Plasticity and Tensile Membrane Action in Lightly-Reinforced Rectangular Concrete Slabs", *Engineering Structures* **138** (2017) pp 195–214.

[13] Kirby, B.R., *"The behaviour of multi-storey steel framed buildings in fire: a European joint research programme"*, British Steel Swinden Technology Centre, 1999.

[14] Wang, Y.C., "Tensile membrane action in slabs and its application to the Cardington fire tests. Fire, static and dynamic tests of building structures", Proceedings of the Second Cardington Conference, England, (1996), pp 55–67.

[15] Newman G.M., Robinson J.T. and Bailey C.G., *"Fire safe design: A new approach to multi-storey steel-framed buildings"*, The Steel Construction Institute, Ascot, UK (2000).

[16] *"BS EN 1992-1-2: 2004: Eurocode 2: Design of concrete structures, Part 1-2: General rules — Structural fire design"*, British Standards Institution, London (2004).

[17] *"BS EN 1993-1-2: 2005: Eurocode 3: Design of steel structures, Part 1-2: General rules — Structural fire design"*, British Standards Institution, London (2005).

[18] *"BS EN 1994-1-2: 2005: Eurocode 4: Design of composite steel and concrete structures — Part 1-2: General rules — Structural fire design",* British Standards Institution, London (2005).

[19] *"BS EN 1991-1-2: 2002: Eurocode 1: Actions on structures Part 1-2: General actions – Actions on structures exposed to fire",* British Standards Institution, London (2002).

[20] Sezen, H. and Setzler, E.J., "Reinforcement slip in reinforced concrete columns", *ACI Structural Journal*, **105** (3), (2008) pp 280–289.

[21] Setzler, E.J., "Modeling the behavior of lightly reinforced columns subjected to lateral loads," MS thesis, Ohio State University, Columbus, OH, 2005, 202 pp.

[22] Sezen, H., "Seismic Behavior and Modeling of Reinforced Concrete Building Columns", PhD thesis, University of California-Berkeley, Berkeley, CA, 2002, 324 pp.

[23] Lynn, A.C., Moehle, J.P., Mahin, S.A. and Holmes, W.T.,"Seismic Evaluation of Existing Reinforced Concrete Building Columns", Earthquake Spectra, EERI, **12** (4), (1996), pp. 715-739.

[24] *"BS 4483:2005: Steel fabric for the reinforcement of concrete. Specification"*, British Standards Institution, London, (2005).

[25] *"BS 4449:2005: Steel for the reinforcement of concrete weldable reinforcing steel, bar, coil and decoiled product"*, British Standards Institution, London, (2005).

[26] Cashell, K.A., "Ultimate behaviour of floor slabs under extreme loading conditions", PhD thesis, Imperial College London, (2009).

[27] Cashell,K.A., Elghazouli, A.Y. and Izzuddin, B.A., "Experimental and analytical assessment of ductility in lightly reinforced concrete members", *Engineering Structures*, **32** (9), (2010) pp. 2729-2743.

[28] Herraiz, B. and Vogel, T., "Novel design approach for the analysis of laterally unrestrained reinforced concrete slabs considering membrane action", *Engineering Structures*, **123**, (2016), pp 313-329.

[29] International Federation for Structural Concrete (*fib*). *fib* Model Code 2010, 1st edition, Ernst & Sohn, Lausanne, (2013).

[30] Kankam, C.K.,"A routine method for measuring bond stress, steel strain and slip in reinforced concrete beams at service loads", Magazine of Concrete Research, **55** (1), (2003) pp. 85–93.

[31] Giroldo, F. and Bailey, C.G., "Experimental bond behaviour of welded mesh reinforcement at elevated temperatures", Magazine of Concrete Research, **60** (1), (2008) pp. 23-31.

[32] Bailey, C.G., "Design of steel structures with composite slabs at the fire limit state", BRE Final Report to the Department of the Environment, Transport and Regions, Building Research Establishment, Garston, UK, 2000.

[33] Bailey, C.G. and Moore, D.B. (2000a), "The structural behaviour of steel frames with composite floor slabs subject to fire - Part 1 Theory", *The Structural Engineer* , **78** (11), pp. 19-27.

[34] Bailey, C.G. and Moore, D.B. (2000b), "The structural behaviour of steel frames with composite floor slabs subject to fire - Part2: Design", *The Structural Engineer*, **78**(11), pp28-33.

[35] Vassart, O. and Zhao, B., "FRACOF: Fire resistance assessment of partially protected composite floors. Design guide", Arcelor Mittal & CTICM (2011).

[36] Clifton, G.C., "Design of multi-storey steel framed buildings with unprotected secondary beams or joists for dependable inelastic response in severe fires", HERA Steel Design & Construction Bulletin, 60, Manukau City, New Zealand (2001).

[37] Omer, E., Izzuddin, B.A. and Elghazouli, A.Y., "Failure of unrestrained lightly reinforced concrete slabs under fire, Part I: Analytical models", *Engineering Structures*, **32**, (2010) pp. 2631-2646.

[38] Omer, E., "Failure of composite steel-concrete slabs under elevated temperatures", PhD. Thesis, Imperial College London, (2006).

[39] Burgess, I.W., Dai, X. and Huang, S.-S., 'An Alternative Simplified Model of Tensile Membrane Action of Slabs in Fire', Proc. Applications of Structural Fire Engineering 2013, Prague, Czech Republic, (2013), pp. 361-368.